

Prompt2DEM: High-Resolution DEMs for Urban and Open Environments from Global Prompts Using a Monocular Foundation Model

Osher Rafaeli^{1a,*}, Tal Svoray^{1a,b}, Ariel Nahlieli^{1a}

^aDepartment of Environmental, Geoinformatics and Urban Planning Sciences, Ben-Gurion University of the Negev, Israel

^bDepartment of Psychology, Ben-Gurion University of the Negev, Israel

Abstract

High-resolution elevation estimations are essential for understanding catchment and hillslope hydrology, analyzing urban morphology and dynamics, and monitoring the growth, decline, and mortality of terrestrial ecosystems. Various deep learning approaches, such as super-resolution techniques and monocular depth estimation, have been developed to generate high-resolution Digital Elevation Models (DEMs). However, super-resolution methods are constrained by fixed upscaling factors, while monocular depth estimation lacks a global elevation context, limiting its applicability for seamless DEM reconstruction. Prompt-based monocular depth estimation, recently introduced, opens new opportunities for extracting absolute elevation in a globally consistent manner. In this work, we present a framework that extends this paradigm to generate high-resolution DEMs from globally available prompts. The method uses low-resolution Shuttle Radar Topography Mission (SRTM) data as prompts and high-resolution RGB imagery from the National Agriculture Imagery Program (NAIP). A vision transformer encoder is fine-tuned using LiDAR-derived DEMs, and a versatile prompting strategy is employed to support tasks such as DEM estimation, void filling, and updating. The proposed framework achieves a 100× resolution enhancement, from 30-m to 30-cm, surpassing previous methods by an order of magnitude. Evaluations across three diverse U.S. landscapes demonstrate robust generalization, accurately capturing urban structures and fine-scale terrain features with < 5 m mean absolute error (MAE) relative to LiDAR, improving over SRTM by up to 18%. Hydrological analyses confirm the framework’s suitability for hazard assessment and environmental monitoring. Finally, we demonstrate its scalability by applying the model to large regions in both the U.S. and Israel. All code and pretrained models are publicly available at this URL.

Keywords: DEM, Vision Transformers, Foundation model, Monocular Depth Estimation

1. Introduction

The digital elevation model (DEM), a commonly used 3D representation of a terrain’s surface that is typically stored as a grid, has widespread environmental applications, including, for example, hydrological and ecological modeling, urban studies, navigation systems, and forest management (Wilson, 2012). DEMs are typically derived from remotely sensed data, such as synthetic aperture radar (SAR), airborne light detection and ranging (LiDAR), and RGB photogrammetry (Guth et al., 2021). These data sources can be used to produce DEMs at various spatial scales, from highly detailed, local topography (Cutler, 2008) to the global scale, e.g., the Shuttle Radar Topography Mission (SRTM), which provides worldwide coverage at a low spatial resolution of 30 m (Rodriguez et al., 2006).

However, environmental studies are currently restricted by the low availability and accessibility of DEMs, which are critical to environmental research. This limitation is rooted in the high costs and relatively limited spatial coverage of large-scale airborne LiDAR surveys (Bhardwaj et al., 2016). Likewise, the more accessible high-resolution alternative, photogrammetric DEMs, requires overlapping optical image pairs and may suffer from stereo-matching problems that can lead to gaps or distortions in the final output (Colomina and Molina, 2014). Consequently, high-resolution DEMs are less accessible to engineers

and researchers in many parts of the world, and typically, they are not updated frequently, thus limiting their usefulness for plot, hillslope and catchment scale applications in environmental monitoring, urban planning, and disaster response (Wang and Menenti, 2021).

In response to the pressing need for high-resolution DEMs (HR-DEMs), super-resolution (SR) approaches have been developed and refined to enhance the spatial resolution of existing DEMs using machine learning (ML) or spatial interpolation techniques Zhang and Yu (2022a). As a next step, super-resolution convolutional neural networks (SRCNNs), super-resolution generative adversarial networks (SRGANs), and super-resolution vision transformers (TTSR) were shown to be able to generate HR-DEMs from low-resolution data sources, significantly outperforming previous spatial interpolation methods (Wang et al., 2024b). More recent studies have explored the integration of auxiliary modal information from remote sensing imagery for deep learning DEM super-resolution, such as shaded relief (Huang et al., 2024), hydrological knowledge (Cao et al., 2025) and relative depth (Huang et al., 2025).

Recent advances in optical sensors and automated analysis algorithms have focused attention on monocular depth estimation (MDE), a computer vision task in which an ML model is used to estimate depth information (Ming et al., 2021). While SR approaches are optimized for pixel-wise similarity, MDE aims to estimate depth values (i.e., distance relative to the sensor) for each pixel given a single (monocular) RGB image (Zhan et al., 2018). MDE models can capture the semantic

*Corresponding author.

Email address: osherr@post.bgu.ac.il (Osher Rafaeli)

structure of a scene, such as recognizing that roads typically exhibit flat and continuous elevation profiles or that buildings possess sharp, vertical discontinuities (Hermann et al., 2020). While MDE models excel at semantic HR depth estimation, their predictions for small patches are local and disconnected from the global elevation context (Florea and Nedeveschi, 2025).

Inspired by the successful use of prompting in foundation vision-language and large language foundation models, the prompt-based monocular paradigm was recently adapted to depth estimation (Lin et al., 2025). The Prompt Depth Anything model (PromptDA) introduced a concise prompt fusion design that integrates low resolution (LR) LiDAR data at multiple scales into a hybrid architecture that combines transformer-based and convolutional layers, the dense prediction transformer (DPT) (Ranftl et al., 2021).

These recent advances have enabled key challenges for DEM predictions to be addressed in both the DEMSR and MDE fields: (1) DEM SR models rely on static inputs tied to a fixed scale factor typically limited to the upscaling resolution (e.g., $4\times - 16\times$) (Yao et al., 2024; Panangian and Bittner, 2024). The output resolution in these models is determined by training data and model architecture rather than by dynamically adapting to the input (Wang et al., 2024a); (2) While MDE methods can produce HR depth maps that match the resolution of the RGB input, prior monocular RGB-based approaches, which lack the absolute values referenced to global elevation and coordinate systems, typically estimate only local elevation (Hong et al., 2025; Cambrin et al., 2024). Consequently, these models often generate patch-based, discontinuous outputs that fail to preserve the spatial continuity necessary for realistic DEM simulation.

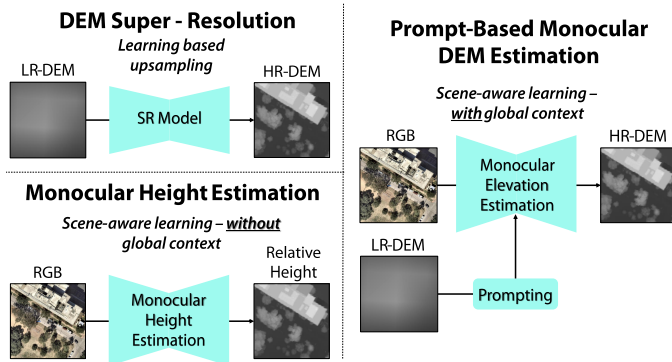


Figure 1: Frameworks for HR-DEM estimation. (Top-left) SR-DEM methods based on interpolating SR elevation maps from LR-DEMs using learned upsampling. (Bottom-left) Monocular elevation estimation to predict relative elevation directly from RGB images, without external elevation input. (Right) Our framework that integrates RGB imagery with LR-DEM prompts to provide global elevation context, which enables absolute HR-DEM estimation through prompt-based monocular learning.

As can be seen in Figure 1, the prompt-based approach can be used as a physical guide to facilitate the integration of MDE with existing elevation information and establish a new paradigm for the enhancement of global DEMs. Such an approach may improve upon previous attempts by an order of magnitude (Panangian and Bittner, 2024; Yu et al., 2025b). This paper, therefore, *aims* to develop a framework to address two critical limitations in current DEM enhancement approaches: *first*, to overcome SR upscaling constraints by enhancing resolution $100\times$ without scale dependencies; and *second*, to pro-

vide MDE with global contextual awareness that ensures spatial consistency across unpatchified predictions while enabling accurate metric elevation estimation. Specifically, three operative objectives were set: (1) to conduct a comprehensive validation with three prompt origins corresponding to three fundamental tasks, including SRTM for HR-DEM estimation from LR-DEM, HR-DEM fused with SRTM for void filling, and HR-digital terrain model (DTM) for DEM updating; (2) to conduct a comprehensive validation across three landscape types—urban, vegetated, and bare terrains—by comparing predictions against HR airborne LiDAR-derived DEMs; and (3) to leverage the model to produce high-resolution, metric-accurate elevation outputs with global context to create seamless, continuous DEMs, first on evaluation sites and ultimately over large parts of the US.

The contributions of this study to the advancement of DEM enhancement methodologies are summarized as follows:

- We introduce an elevation-prompted monocular foundation model for the first time.
- We leverage freely available SRTM DEMs as absolute-height prompts, ensuring a globally consistent elevation context.
- We leverage patch-wise MDE predictions into seamless DEMs that are ready for slope, aspect, and hydrological analyses.

2. Materials and Methodology

2.1. Study area and dataset

To examine the proposed framework, we agglomerated a dataset from publicly available sources for model training, evaluation and application. These include: (1) HR RGB imagery from the National Agriculture Imagery Program (NAIP) (U.S. Geological Survey, 2025); (2) global 30-m SRTM LR elevation data (NASA Shuttle Radar Topography Mission (SRTM), 2013); and (3) HR LiDAR-derived DEMs obtained from the OpenTopography platform (ope, 2025). The dataset covers several environments in the US, and is consistent across three representative landscapes: urban, vegetated natural terrain, and bare natural terrain. For each type of landscape, two sites were selected: one for training and the other for testing (Figure 2 and Table 1).

For the urban setting, two cities with publicly available HR LiDAR data were selected: Austin, Texas ($30.2933^\circ, -97.7733^\circ$), (Passalacqua, 2015), and Provo, Utah ($40.3345^\circ, -111.7383^\circ$), (uta, 2025). The vegetated natural environment is represented by Kelsey Peak ($40.4580^\circ, -112.3644^\circ$) (lak, 2025) and Diamond Fork Canyon ($40.1047^\circ, -111.4355^\circ$), both of which are in Utah (Jones, 2018). The bare, or sparsely vegetated, environment is represented by Chaco Canyon in north-western New Mexico ($36.0544^\circ, -107.9470^\circ$) (Dorshow, 2019) and by the Casa Diablo Mountain zone in the California desert ($37.5919^\circ, -118.5232^\circ$) (bis, 2025).

The three landscape types represented here were characterized by variations in elevation. Urban landscapes exhibited more bimodal slope distributions. The ground-level surface was uniform due to human land use, such as roads and pavement, while buildings and trees created high slopes at the edges.

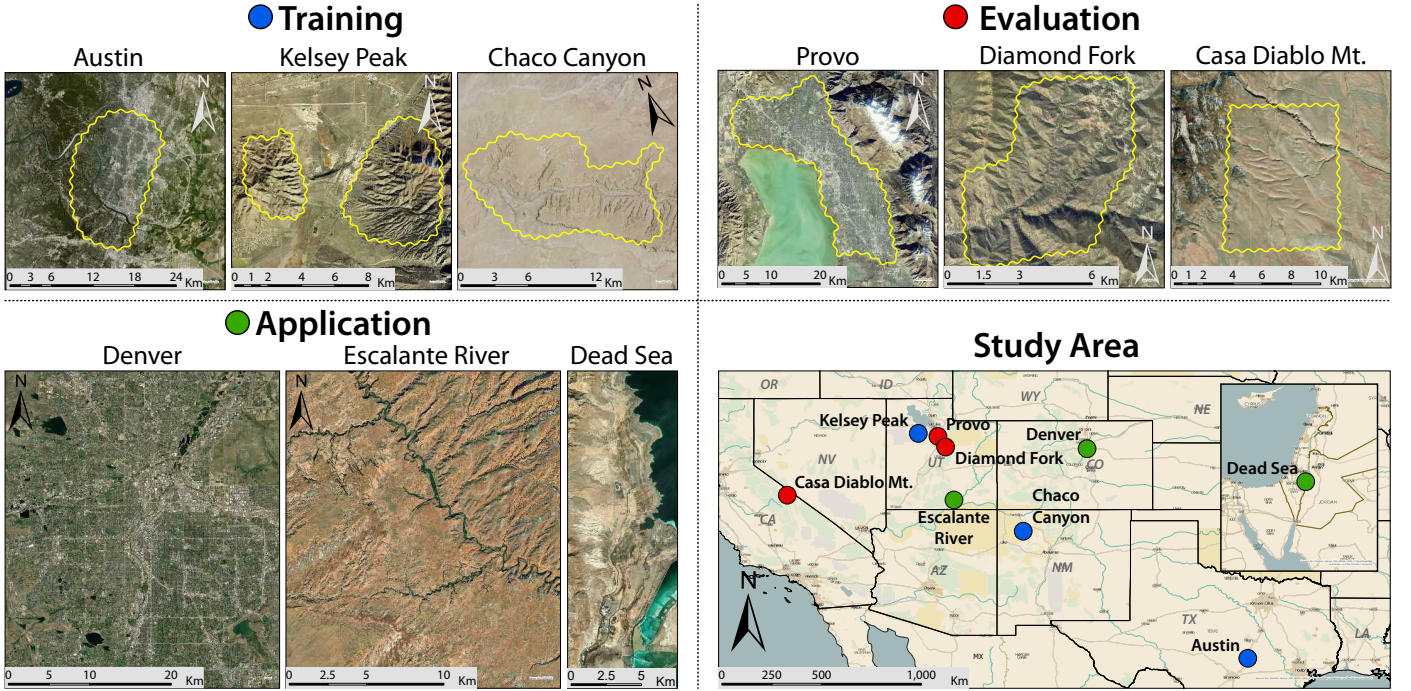


Figure 2: Our study sites for training and evaluation are located in four different states in the United States. For urban regions, we selected Austin, Texas, and Provo, Utah. For natural vegetated areas, we used Kelsey Peak and Diamond Fork Canyon in Utah. For natural, bare sites, we used Chaco Canyon in New Mexico and Casa Diablo Mountain in California. For model application, we used Denver in Colorado, the Escalante River in Utah, and the Dead Sea in Israel as representative urban, natural vegetated and natural bare sites, respectively.

Table 1: Summary of the datasets used for elevation estimation across six study sites.

Site	Landscape Type	RGB (NAIP)	LiDAR DEM	SRTM DEM	Area (km ²)
Austin, TX	Urban	60 cm/px	50 cm/px	30 m/px	157
Provo, UT	Urban	60 cm/px	50 cm/px	30 m/px	228
Kelsey Peak, UT	Natural Vegetated	60 cm/px	50 cm/px	30 m/px	22
Diamond Fork Canyon, UT	Natural Vegetated	60 cm/px	50 cm/px	30 m/px	22
Chaco Canyon, NM	Natural Bare	60 cm/px	50 cm/px	30 m/px	70
Casa Diablo Mountain, CA	Natural Bare	60 cm/px	1 m/px	30 m/px	40

Table 2: Statistical metrics of elevation distribution for DEMs across six study sites. Slope statistics are shown in parentheses with units in degrees (°), while elevation units are in meters (m).

Site Elevation	Mean (m)	Std (m)	Skewness	Kurtosis	Bimodality Coefficient
Austin, TX	207.35 (54.94°)	35.01 (25.78°)	0.24 (-0.87)	2.67 (2.33)	0.396 (0.755)
Provo, UT	1438.37 (34.16°)	78.63 (29.25°)	2.35 (0.34)	10.72 (1.47)	0.607 (0.761)
Kelsey Peak, UT	1863.03 (61.32°)	194.32 (13.23°)	0.55 (-1.30)	2.25 (4.40)	0.581 (0.612)
Diamond Fork Canyon, UT	1950.41 (59.73°)	228.44 (17.46°)	0.00 (-1.02)	2.11 (3.44)	0.475 (0.592)
Chaco Canyon, NM	1943.40 (19.92°)	46.47 (18.67°)	1.37 (1.51)	4.95 (4.67)	0.579 (0.703)
Casa Diablo Mountain, CA	1701.39 (32.23°)	139.57 (16.27°)	0.30 (0.88)	2.27 (3.33)	0.481 (0.532)

Austin was more vegetated, and therefore, more sharp slopes were obtained due to high trees. This can be visually confirmed in the slope histograms (see Figure 3). The city of Provo showed greater elevation bimodality (0.607) and skewness (2.35), suggesting a long-tailed and peaked distribution indicating that the different city regions, one with moderate hilly terrain and the other the lower lake shore, had different elevation levels. For Austin, in contrast, a skewness value of 0.24 and a bimodality of 0.40 were obtained, suggesting a nearly symmetric distribution of elevation data due to more homoge-

neous terrain.

The generally lower variability between the peaks and valleys of the elevation distribution in urban landscapes resulted in a lower standard deviation (Austin: 35.01 m, Provo: 78.63 m) compared to the natural landscapes. These showed a larger standard deviation of elevation values, even for smaller areas. In our dataset, the natural vegetated areas were steeper, with Diamond Fork Canyon and Kelsey Peak in Utah showing high mean elevation values and large standard deviations (194–228 m) indicating irregular mountainous terrain. The value of the

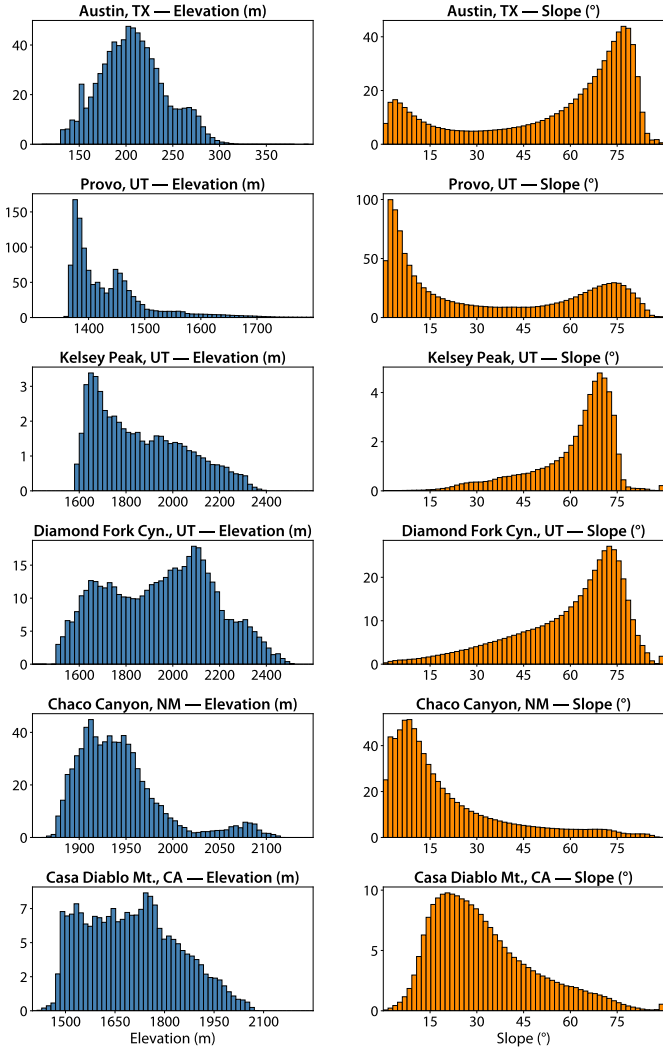


Figure 3: Histograms of elevation and slope across the six study sites indicate that urban and naturally vegetated regions generally have steeper slopes compared to bare terrain.

mean slope in Diamond Fork Canyon was 59.73° , and in Kelsey Peak, it was 61.32° . Although the mean slope were high, the low standard deviation of less than 20° indicates that the terrain was more uniform.

Both Chaco Canyon, NM, and Casa Diablo Mountain, CA, exhibited lower variability in elevation values than vegetated areas in Utah. In particular, the skewness and kurtosis of Chaco Canyon were higher due to the asymmetry between the steep canyon and the plateau. The mean slope was 19.92° , with a bimodal distribution resulting from the contrast between the broad plateaus and the steep canyons. A smoother distribution of elevation values was obtained for Casa Diablo, which features more uniform terrain and broad hillslopes, with a mean slope of 32.23° . The standard deviation of the slope was higher than in the vegetated sites due to steep narrow canyons and stream incisions (Figure 3 and Table 2).

All elevation and NAIP datasets were geo-referenced and co-registered according to the North American Datum (NAD) of 1983 UTM coordinate system (Federal Geographic Data Committee, 1998). Each landscape type was divided into two similar subset sites, one for training and the other for evaluation. Specifically, Austin, Kelsey Peak, and Chaco Canyon were used to fine-tune the model. These locations were chosen as repre-

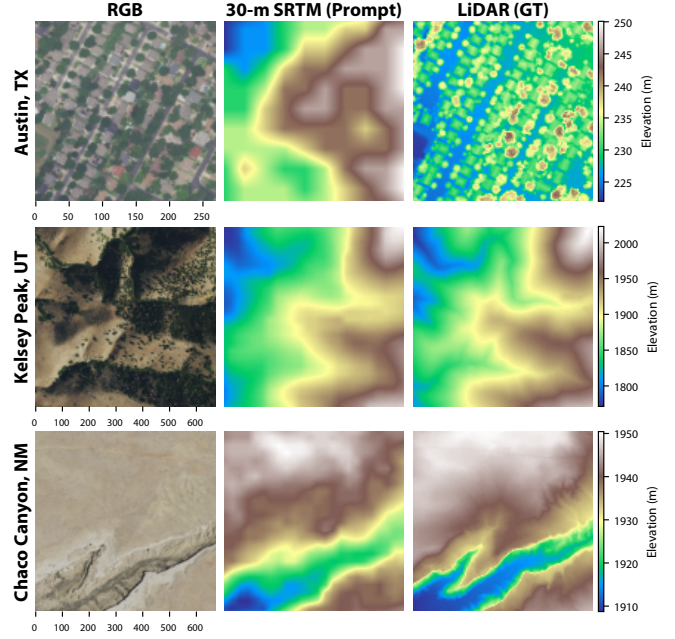


Figure 4: Sample patches from the training dataset include NAIP RGB imagery, SRTM data as prompts, and high-resolution LiDAR DEMs as ground truth.

sentative examples from different regions to create a balanced train-test split. The objective was to ensure that the model was trained on a variety of terrains to perform a more comprehensive evaluation without overfitting the model to a single type of landscape.

The application phase was conducted in large-scale regions where 50-cm LiDAR DEMs are unavailable with the objective of generating novel, deep learning-based HR-DEMs. Three study areas were selected: Denver, Colorado ($\sim 1,800 \text{ km}^2$), which has newly available 30-cm NAIP data; the Escalante River watershed, a tributary of the Colorado River, in Utah (474.69 km^2), with standard 60-cm NAIP imagery; and the Dead Sea shore in Israel, where SRTM and high-resolution 15-cm orthomosaic data have been available since 2023. The Dead Sea region is known for its salt-induced sinkholes (Rafaeli et al., 2025).

In addition to the main experiment on the SRTM-LiDAR dataset, the proposed framework was compared with DEM super-resolution (DEMSR) methods. To that end, a recently introduced dataset, the DEM-OPT-Depth SR Dataset, was used. This publicly available test set contains 5-m RGB, 30-m LR-DEM, and 7.5-m HRDEM data. We fine-tuned the data using only 33% (231 samples) and tested it on the remaining 67% (500 samples) (Huang et al., 2025). The Results section of this paper reports metrics from the original MFSR paper together with the results of our model’s performance on the DEM-OPT-Depth SR Dataset.

2.2. Model architecture

Current depth foundation models (Yang et al., 2024a; Birkl et al., 2023a) generally share similar network structures to dense prediction transformer (DPT) (Ranftl et al., 2021) networks. Specifically, they use a vision transformer (ViT) with multiple stages to extract tokenized image features that represent the feature map at each stage.

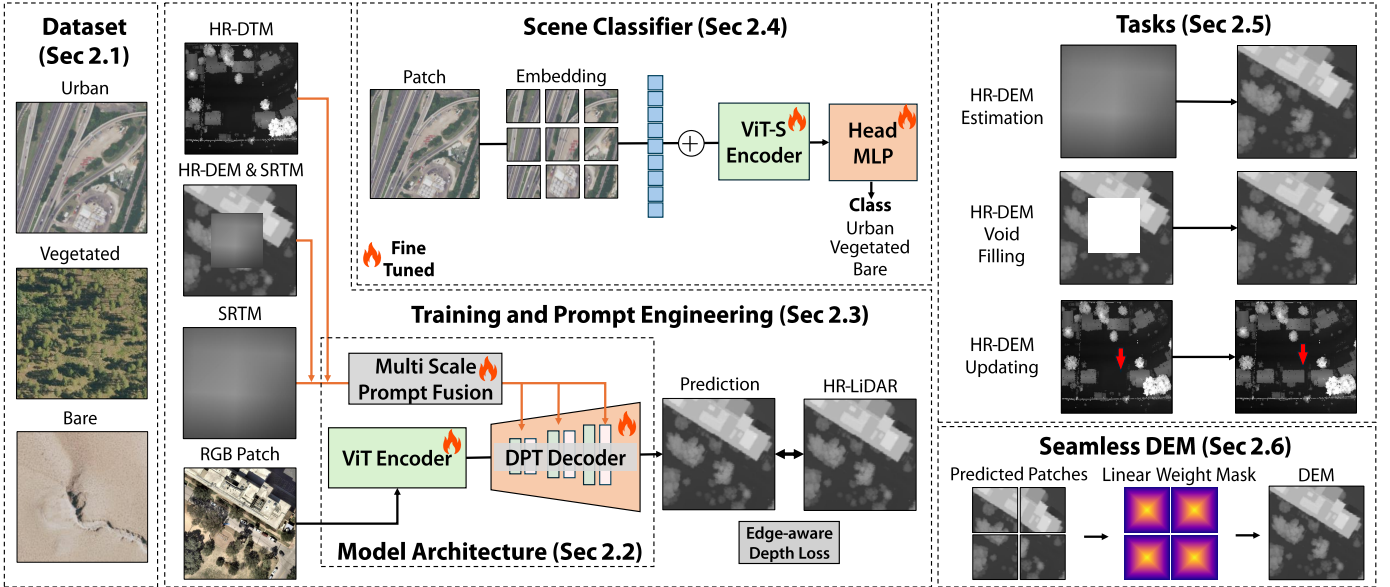


Figure 5: Proposed Prompt2DEM Framework: Dataset - Landscape categories – The model was trained and evaluated on three landscape types: urban, natural vegetated, and natural bare land. Training and prompt engineering – All model components were fine-tuned using NAIP 3-channel (RGB) aerial images with three different prompt types: LR-SRTM, HR-DEM from LiDAR (with holes filled using SRTM), and HR-DTM extracted from HR-digital surface model (DSM). Scene Classifier - a lightweight scene classifier to categorize NAIP image patches prior to prediction. Seamless DEM creation – Each patch was multiplied by a linear mask that assigns higher weights to the center of the patch and gradually decreasing weights toward the edges. This mitigates edge artifacts and ensures smooth transitions between overlapping patches. Inference tasks – During inference, the model was evaluated on three core tasks: HR-DEM estimation, void filling, and updating.

ViT Encoder — In the proposed framework, we used a pre-trained ViT encoder from the Depth Anything V2 model, which builds on the largest DINOv2 and leverages its inherent generalization ability (Yang et al., 2024c). In particular, Depth Anything V2 introduces several key training advantages: (1) It overcomes the limitations of manual image annotation by incorporating synthetically annotated data during training, with fine-detailed labels; (2) It employs a teacher-student architecture to obtain a lightweight yet accurate model. The model is initially trained on synthetic images, after which the teacher model generates pseudo masks on unannotated real images. Finally, a smaller student model is trained on these pseudo-annotated images; (3) Its annotation pipeline integrates SAM for image sampling, utilizing a combination of real and pseudo-labeled depth maps derived from 62 million images (Yang et al., 2024b).

Depth Anything V2 is benchmarked on standard datasets such as KITTI, Sintel, and others, and it outperforms previous foundation MDE models, including MiDaS v3.1 from Intel Labs (Birkel et al., 2023b). Its superior performance is further demonstrated on the DA-2K dataset, which includes eight different image categories, 9% of which consist of aerial and fine-detail imagery

DPT Decoder — The DPT decoder reassembles features from different stages into image-like representations using the reassemble operation. Finally, a sequence of convolutional blending steps is applied to merge features across different stages and produce a dense depth map, to produce full resolution predictions using a convolutional decoder. For monocular depth estimation, we observe an improvement of up to 28% in relative performance when compared to a state-of-the-art fully-convolutional network. Ranftl et al. (2021).

Prompt Fusion Block — PromptDA proposes a concise prompt-fusion architecture that is tailored for a DINOv2 en-

coder, a DPT-based decoder, and a prompt injection mechanism to enable the integration of low-resolution (LR) depth information (Lin et al., 2025). Prompts are bilinearly resized to match the current scale of the spatial dimensions $R \in \mathbb{R}^{1 \times H_i \times W_i}$. The resized depth map is then passed through a shallow convolutional network to extract depth features. These are projected to match the channel dimensions of image features $F_i \in \mathbb{R}^{C_i \times H_i \times W_i}$ using a zero-initialized convolutional layer. Subsequently, depth features are added to intermediate features of the DPT decoder for depth prediction, see Fig 6.

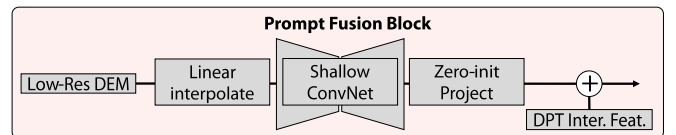


Figure 6: Architecture of the Prompt Fusion Block. The low-resolution DEM is linearly interpolated, passed through a shallow convolutional network, and projected via a zero-initialized layer. The result is added to the intermediate DPT features to inject elevation context into the dense prediction transformer.

2.3. Training and prompt engineering

Typically, training a prompt-based monocular model requires LR depth information as prompts and precise ground truth (GT) depth for backpropagation. Here, because the data are transitional to elevation values, we trained the model using (1) the global DEM 30-m SRTM, and (2) HR LiDAR-derived DEMs (50 cm and 1 m). For accurate predictions, we unfroze all weights during the initial training. This step was needed because the pretrained weights of the PromptDA model were trained on ground photography, captured by iPhone devices, and prompted with low-resolution depth data from the iPhone’s

LiDAR sensor. Moreover, the prompts we used are fundamentally different because surface elevation data use positive values, i.e., above mean sea level. In contrast, MDE is typically used to estimate camera-object distances. A sample of training patches is shown in Fig. 4.

The final fine-tuning stage was performed in three steps using different prompts to achieve high accuracy across the three proposed tasks. (1) For HR-DEM estimation, we used the coarse 30-m SRTM data as prompts combined with HR RGB imagery (NAIP) and detailed LiDAR-derived DEMs. This training loop, specifically designed for surface elevation estimation, was conducted for 10 epochs. (2) For the void-filling task, we designed prompts consisting of HR-DEMs with a central square hole that was filled using SRTM data. The hole was fixed to half the patch size and centrally located, while the model was trained to predict the complete HR-LiDAR DEM. (3) For DEM updating, we generated digital terrain model (DTM) patches that excluded surface features in urban landscapes. These were used as prompts to predict HR-DSMs, simulating a DEM updating task where new structures in recently captured RGB images are reflected in elevation data. The void-filling and updating tasks were fine-tuned for only 5 epochs using weights initialized from the initial training with raw SRTM prompts.

In total, seven models were trained: DEM estimation and void-filling models for each of the three landscape types: urban, natural vegetated, and natural bare soil, and an urban-specific DEM updating model in which DSM–DTM differences are more significant and changes occur more frequently due to human activity.

2.4. Scene classifier

To facilitate automated execution of the framework pipeline, at the inference stage, we designed a lightweight scene classifier to categorize NAIP image patches prior to prediction. This was implemented to enable dynamic adjustment of the model weights during large-scale applications of the model, when the landscape can change significantly. This step allows for automatic operation and enables the model to select the most suitable weights for each patch, ensuring that the correct pre-trained MDE model is used for each scene, i.e., urban, vegetated, or bare.

The classifier works by splitting the input image into non-overlapping patches, each of which is flattened and projected into an embedding vector. These patch embeddings are then fed into a transformer encoder composed of multi-head self-attention layers (MLP). For efficiency, we selected a lightweight backbone, a small vision transformer (ViT-S) with 16×16 patches.

Our results from evaluations of 1,000 unseen patches from each scene are provided here as intermediate findings. Excelling in scene classification, this model achieved F1-scores of 0.95, 0.93, and 0.97 for the Urban, Vegetated and Bare classes, respectively. We therefore integrated this lightweight classifier into our framework to automatically select the most appropriate pre-trained model for each patch.

2.5. Tasks

After model training, the evaluation step in the proposed framework comprises three tasks: (1) HR-DEM estimation with a prompt of a 30-m SRTM image, the output of which is a predicted DEM with a spatial resolution of 60 cm aligned with

the NAIP RGB input; (2) DEM void filling with the HR-DEM prompt, with holes filled using SRTM; and (3) DEM updating with the model prompted with the unupdated HR-DEM and the updated NAIP imagery.

2.6. Seamless DEM reconstruction

Since each patch is predicted separately due to computer resource limitations, directly stitching the patches together can create visible discontinuities between patches, which may negatively affect downstream DEM analyses such as flow accumulation and stream network extraction. To ensure smooth transitions between patches, we implemented a distance-based linear blending method for overlapping regions (Richardt et al., 2013). This technique assigns higher weights to image pixels that are farther from the patch edges and lower weights to pixels near the edges of the patch. Overlapping areas are then combined using these spatially varying weights, ensuring a seamless mosaic and mitigating boundary artifacts.

Specifically, for each patch, a 2D linear mask is constructed by computing the minimum normalized distance from each pixel to the patch boundaries. This mask increases smoothly from 0 at the patch boundaries to 1 at its center, promoting gradual transitions in overlapping areas. The final blended value at each pixel is obtained as a weighted average of all overlapping patches using the corresponding weights (see Fig. 5).

2.7. Evaluation metrics

Two commonly used elevation error evaluation metrics, the mean absolute error (MAE) and the root mean square error (RMSE), were used, as shown in Eqs. 1 and 2:

$$\text{MAE} = \frac{1}{N} \sum_{i=1}^N |y_i - \hat{y}_i|, \quad (1)$$

$$\text{RMSE} = \sqrt{\frac{1}{N} \sum_{i=1}^N (y_i - \hat{y}_i)^2}, \quad (2)$$

where y_i denotes the pixel value of the original DEM, \hat{y}_i denotes the corresponding pixel value of the filled DEM, and N is the number of void pixels.

Since the slope of the surface is closely related to relative elevation accuracy, we also calculated the RMSE for the similarity between the values of the slope and the aspect. The two variables were calculated using the following equations:

$$\text{Slope} = \sqrt{\left(\frac{\partial z}{\partial x}\right)^2 + \left(\frac{\partial z}{\partial y}\right)^2}, \quad (3)$$

$$\text{Aspect} = \tan^{-1} \left(\frac{\frac{\partial z}{\partial y}}{\frac{\partial z}{\partial x}} \right), \quad (4)$$

where $\frac{\partial z}{\partial x}$ and $\frac{\partial z}{\partial y}$ represent the partial derivatives of the elevation values in the x and y directions, respectively.

To assess the relevance of the predicted DEMs to hydrological applications (Svoray et al., 2021), we extracted stream networks using the 8D flow model (Svoray, 2004), which included the Fill, Flow Direction, and Flow Accumulation tools in ArcGIS Pro. The resulting stream maps were compared with ground truth using common binary segmentation metrics, i.e.,

Intersection over Union (IoU), precision, recall, F1-score, and overall accuracy, as defined below:

$$\text{IoU} = \frac{|A \cap B|}{|A \cup B|} \quad (5)$$

$$\text{Precision} = \frac{TP}{TP + FP} \quad (6)$$

$$\text{Recall} = \frac{TP}{TP + FN} \quad (7)$$

$$\text{F1 Score} = 2 \times \frac{\text{Precision} \times \text{Recall}}{\text{Precision} + \text{Recall}} \quad (8)$$

$$\text{Accuracy} = \frac{TP + TN}{TP + TN + FP + FN}, \quad (9)$$

where TP, TN, FP, and FN denote, respectively, true positive, true negative, false positive, and false negative values, and A and B are predicted and ground truth segments, respectively.

2.8. Technical details

During the training process, the batch size was set to 2 using a single NVIDIA RTX A4000 GPU. We used the Adam optimizer with a learning rate of $5e-5$. The loss function was a composite of the standard L1 loss and an edge-aware term to supervise both the predicted elevation (\hat{E}) and its spatial gradients. The edge loss weight λ was set to 0.9. The overall loss function is defined as:

$$\mathcal{L}_{\text{edge}} = \mathcal{L}_1(E_{\text{gt}}, \hat{E}) + \lambda \cdot \mathcal{L}_{\text{grad}}(E_{\text{gt}}, \hat{E}), \quad (10)$$

where the gradient loss term is calculated as:

$$\mathcal{L}_{\text{grad}}(E_{\text{gt}}, \hat{E}) = \left| \frac{\partial(\hat{E} - E_{\text{gt}})}{\partial x} \right| + \left| \frac{\partial(\hat{E} - E_{\text{gt}})}{\partial y} \right|. \quad (11)$$

3. Results

The performance of the prompt-based framework was evaluated by comparing absolute terrain feature errors between predicted DEMs, SRTM, and HR-LiDAR reference data. The results show that the predicted DEM maintained the spatial resolution of the input RGB imagery (0.6 m), which provided substantially greater amounts of more valuable detail than was provided by the SRTM data (Figures 7, 8, and 9).

3.1. HR-DEM estimation

Table 3 shows the evaluation metrics across the three types of landscape, i.e., urban, natural vegetated, and natural bare areas. The predicted DEM consistently outperformed the baseline SRTM data in almost all landscape types compared to the HR-LiDAR data.

In the urban landscape, the predicted DEM reduced the error from MAE from 2.769 m (SRTM) to 2.377 m, and the error from RMSE was reduced from 3.434 m to 3.258 m. Similar improvements were observed in calculated slope (MAE: 13.548° vs. 14.324°; RMSE: 22.602° vs. 24.443°), while the aspect MAE improved only slightly (113.917° vs. 114.924°), and its RMSE worsened slightly (146.918° vs. 144.909°).

In the vegetated landscape, the initial SRTM error was more significant, and therefore, the advantage of the predicted DEM

was even more noticeable. This was especially true for the elevation and slope estimations: the MAE dropped by almost 1 m from 5.661 m to 4.645 m, and the RMSE decreased from 7.275 m to 5.928 m. The MAE and RMSE of the slope also improved, but the RMSE of the aspect was virtually the same.

For bare soil landscapes, the SRTM error was initially small in both cases of elevation, and the slope errors were lowest in all types of landscape. Yet the accuracy of the predicted DEM was higher (elevation MAE: 2.132 m vs. 2.217 m; RMSE: 2.695 m vs. 2.871 m). The RMSE of the slope improved slightly, and the aspect errors were markedly reduced (MAE: 60.269° vs. 63.505°; RMSE: 101.345° vs. 104.144°).

The metrics compared indicate that, in general, the prompt-based framework significantly improved the absolute accuracy of the DEM, and this effect was more noticeable in the vegetated and urban landscapes, although it also performed well in the simpler, bare soil landscapes (Figures 7A, 8A and 9A).

3.2. HR-DEM void filling

Table 4 shows the accuracy metrics for DEM void filling in the urban, vegetated, and bare landscapes. For void filling, we used a fusion prompt that comprised HR LiDAR with hole-filled SRTM. The metrics are calculated for the filled area. The results show that the filled area consistently outperformed the baseline SRTM data in almost all types of landscape compared to HR-LiDAR ground truth data.

In the urban landscape, the MAE of the predicted DEM decreased from 2.792 m in SRTM to 1.860 m. The RMSE similarly declined in the same direction from 3.397 m to 2.706 m. Comparable improvements in the predicted DEM were observed in calculated slope (MAE: 13.624° vs. 14.475°; RMSE: 22.368° vs. 24.156°). For the aspect, MAE improved slightly (112.155° vs. 114.843°), and RMSE was even worsened slightly by the predicted DEM (144.814° vs. 144.253°).

The predicted DEM exhibited better performance in the vegetated landscape, where the inherent limitations of the SRTM resulted in larger baseline errors. This advantage was most evident in elevation accuracy and slope calculations, for which the MAE dropped from 5.698 m to 4.927 m, and the RMSE declined from 7.215 m to 6.198 m. Similar improvements were observed in slope metrics, for which both the MAE and the RMSE were substantially reduced compared to the SRTM. However, the RMSE of the aspect was virtually unchanged.

For bare soil landscapes, initially small errors were observed in the SRTM data, with both elevation and slope showing the lowest error values in all evaluated landscapes. However, the predicted DEM was more accurate (elevation MAE: 1.934 m vs. 2.240 m; RMSE: 2.845 m vs. 2.475 m). The slope and aspect improved slightly (slope - MAE: 2.710° vs. 2.799°; RMSE: 3.3871° vs. 4.124°; aspect - MAE: 62.821° vs. 63.206°; RMSE: 100.728° vs. 100.725°).

A comparative analysis of the different types of landscape showed that the accuracy of the elevation estimates was optimal in the urban and bare soil landscapes. In the vegetated landscapes, however, the elevation estimation was slightly less accurate relative to the DEM estimation benchmark. The improved accuracies of the slope and aspect estimations in vegetated areas paralleled those observed in the primary DEM estimation task. See Figures 7B, 8B, and 9B.

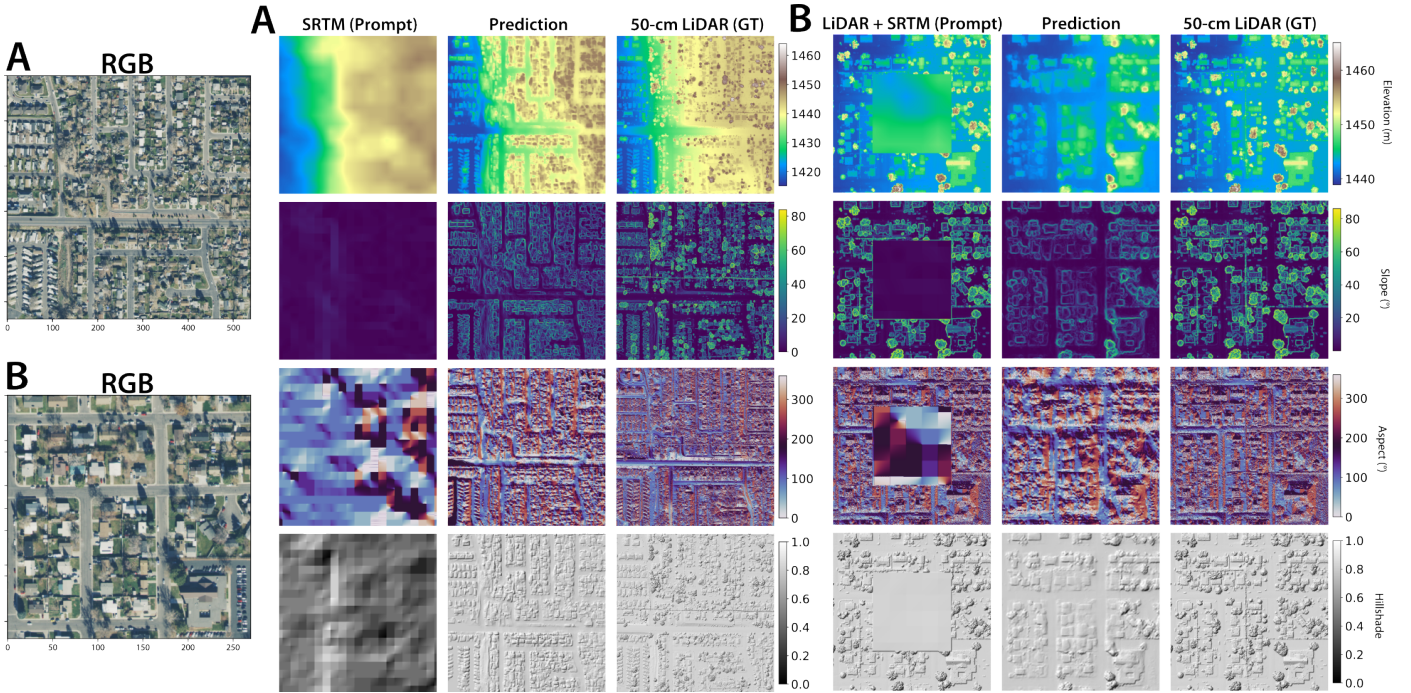


Figure 7: Visual Evaluation – (A) DEM estimation in a natural vegetated environment: elevation in meters, slope in degrees, aspect in radial direction, and hillshade visualization. The global SRTM general terrain was preserved for elevation prediction, while RGB information added building footprints and urban trees, which are clearly visible in the slope, aspect, and hillshade maps. (B) DEM void filling in an urban environment prompted by HR-DEM with SRTM: the predicted extracted elevation was seamless, while regions prompted by HR-DEM showed fine features such as trees, which are visible in the slope and hillshade maps, reconstructed with better accuracy.

Table 3: Evaluation metrics for DEM estimation task across different landscape types. Predicted DEM and SRTM vs. LiDAR ground truth data across landscape types.

		Urban		Vegetated		Bare	
		Predicted DEM	SRTM	Predicted DEM	SRTM	Predicted DEM	SRTM
Elevation (m)	MAE	2.377	2.769	4.645	5.661	2.132	2.217
	RMSE	3.258	3.434	5.928	7.275	2.695	2.871
Slope (°)	MAE	13.548	14.324	17.762	19.033	2.721	2.860
	RMSE	22.602	24.443	23.537	24.938	4.415	4.694
Aspect (°)	MAE	113.917	114.924	81.039	83.065	60.269	63.505
	RMSE	146.918	144.909	120.246	120.279	101.345	104.144

Table 4: Evaluation metrics for void-filling task across different landscape types. Elevation and terrain attributes from predicted DEM and SRTM were compared to LiDAR ground truth data.

		Urban		Vegetated		Bare	
		Predicted DEM	SRTM	Predicted DEM	SRTM	Predicted DEM	SRTM
Elevation (m)	MAE	1.860	2.792	4.927	5.698	1.934	2.240
	RMSE	2.706	3.397	6.198	7.215	2.475	2.845
Slope (°)	MAE	13.624	14.475	17.274	19.004	2.710	2.799
	RMSE	22.368	24.156	22.553	24.781	3.871	4.124
Aspect (°)	MAE	112.155	114.843	79.950	81.660	62.821	63.206
	RMSE	144.814	144.253	117.162	116.732	100.728	100.725

3.3. HR-DEM updating

The DEM updating task used terrain-filtered prompts extracted from the HR reference DTM to evaluate model updating capabilities. The evaluation was conducted in an urban landscape (Provo), in which substantial surface differences were observed between the DTM and the original DEM due to the presence of buildings. While MAE and RMSE values were lower when using DTM prompts, when using the model-predicted DEM, higher accuracy was achieved via the enhanced reconstruction of surface features. slope estimation was better than

the DTM baseline, while aspect calculations were comparable to those obtained from DTM prompts. Nevertheless, the predicted DEM consistently outperformed the predictions derived from the SRTM prompts in all metrics evaluated (see Fig. 10).

Table 5 shows the evaluation metrics for the performance of the DEM updating task in the urban landscape. The predicted DEM reduced elevation errors from MAE from 1.840 m (SRTM) to 1.744 m, and it reduced those from RMSE from 3.491 m to 3.111 m. Similar improvements were obtained in the slope (MAE: 16.894° vs. 17.262°; RMSE: 27.074° vs.

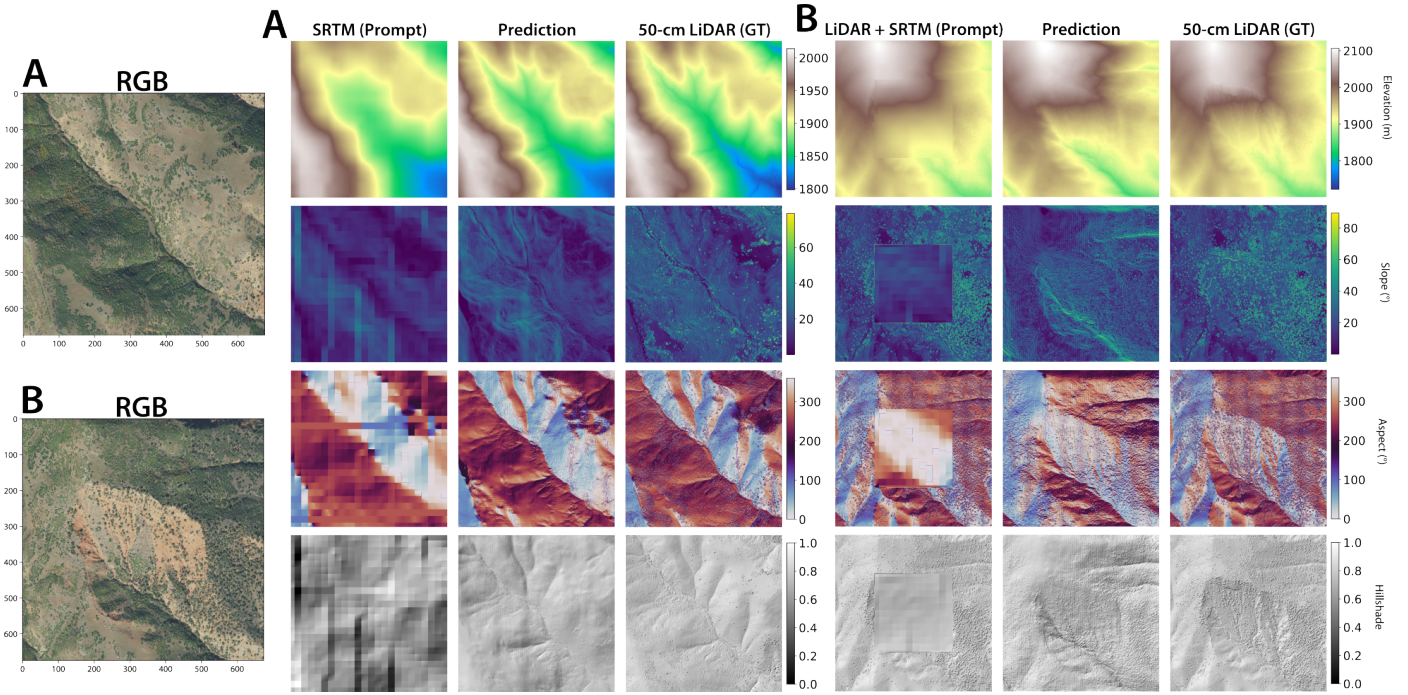


Figure 8: Visual Evaluation - (A) DEM estimation in natural vegetated landscape, elevation in meters, slope in degrees, aspect in radial direction, and hillshade visualization. The global SRTM general terrain was preserved for elevation prediction, while RGB information added detailed terrain features, such as small streams that are clearly visible in the slope, aspect, and hillshade maps. (B) DEM void filling in a natural vegetated landscape prompted by HR-DEM with SRTM: the predicted extracted elevation was seamless, while regions prompted by HR-DEM showed fine features, such as trees, reconstructed with better accuracy, which are visible in the slope and hillshade maps.

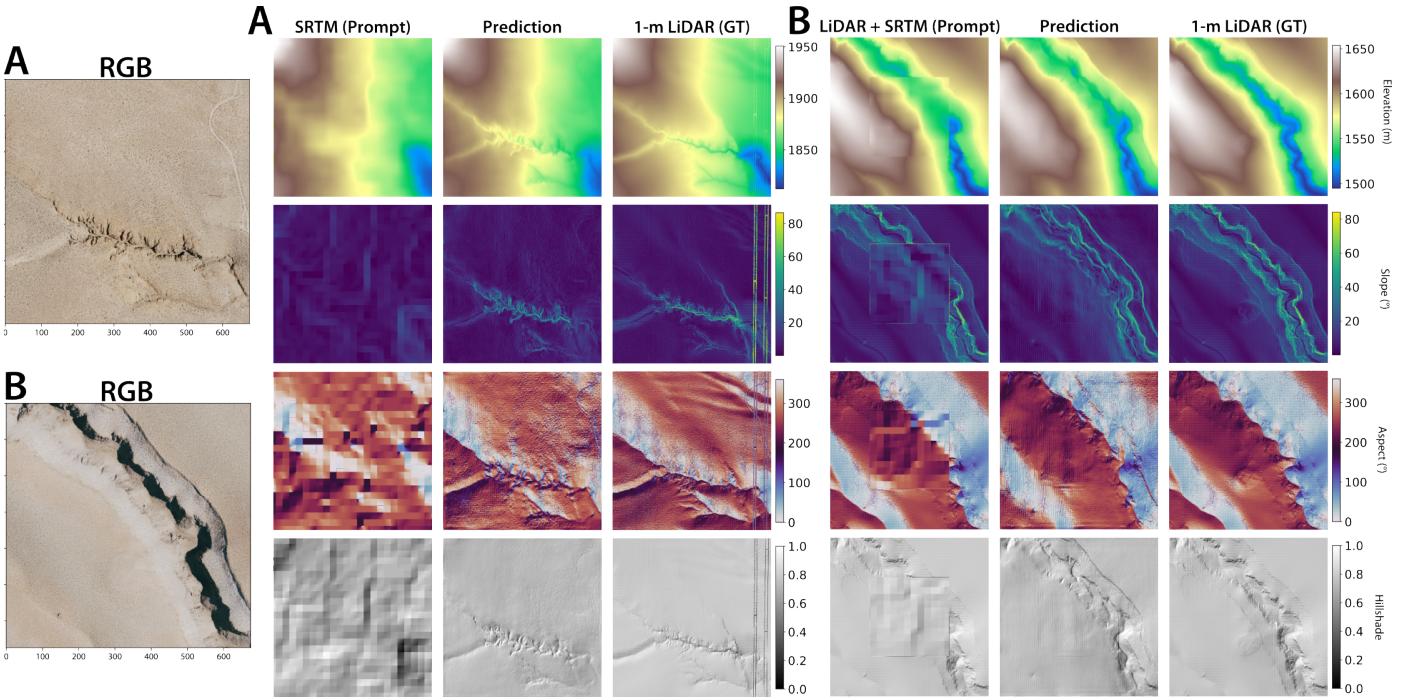


Figure 9: Visual Evaluation - (A) DEM estimation in natural bare landscape, elevation in meters, slope in degrees, aspect and radial direction, and hillshade visualization. The global SRTM general terrain was preserved for elevation prediction, while the RGB information added detailed terrain features, such as small streams which are clearly visible in the slope, aspect, and hillshade maps. (B) DEM void filling in bare landscape prompted by HR-DEM with SRTM: the predicted extracted elevation was seamless, while in regions prompted by HR-DEM, the slope and aspect maps were more accurate.

28.312°), while the RMSE of the aspect worsened slightly for the predicted DEM (135.841° vs. 127.204°).

3.4. Seamless DEM

Stream network accuracy metrics for natural vegetated landscapes are presented in Table 6, while the corresponding metrics for bare landscapes are shown in Table 7. Seamless DEM reconstruction was achieved by unpatchifying predicted patches

Table 5: Evaluation metrics for the DEM updating task on the urban landscape prompted by HR DTM. Predicted DEM compared to LiDAR DSM data.

		Predicted DEM	LiDAR DTM
Elevation (m)	MAE	1.744	1.840
	RMSE	3.111	3.491
Slope (°)	MAE	16.894	17.262
	RMSE	27.074	28.312
Aspect (°)	MAE	101.113	87.502
	RMSE	135.841	127.204

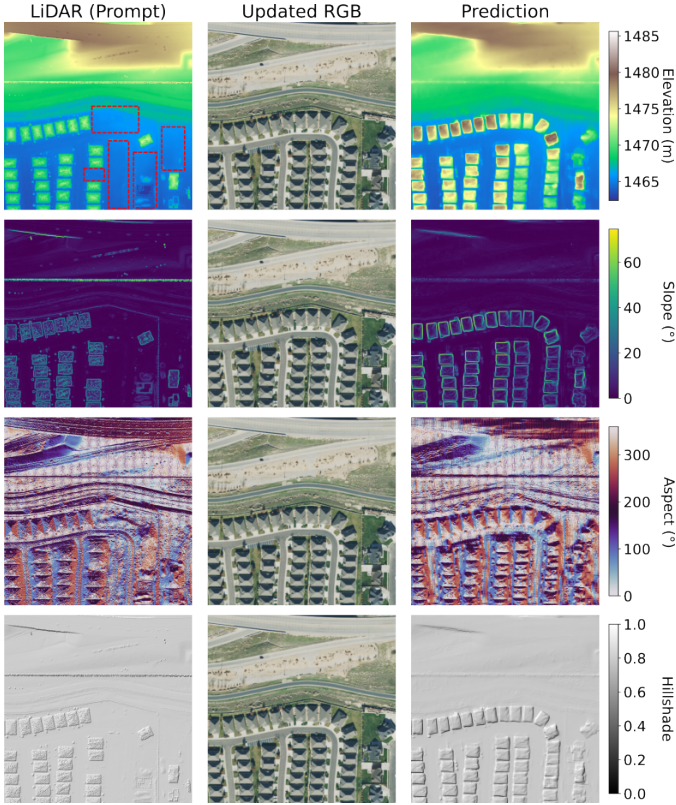


Figure 10: Visual Evaluation – DEM updating in an urban landscape includes elevation (in meters), slope (in degrees), aspect (in radians), and hillshade visualization. As shown in the red rectangles, the buildings that were missing in the original RGB (unupdated) image were successfully reconstructed by using the unupdated LiDAR prompt together with the updated RGB imagery. This approach allowed missing features to be restored while maintaining high accuracy compared to the HR-DEM prompt.

using a distance-based linear blending method. The resulting seamless DEMs for both sites are visualized in Figures 11 and 12. Stream networks were calculated in ArcGIS Pro and were compared with channel networks extracted from both SRTM and HR-LiDAR DEMs. Relative to the LiDAR data, the performance of the predicted DEM was consistently superior to that of the SRTM baseline data in almost all types of landscape.

According to the metrics in Table 6, the predicted DEM in vegetated landscapes provided a more accurate stream network compared to SRTM. This is evident from the IoU of extracted streams: the predicted DEM increased the IoU from 0.1265 to 0.3695. Similar improvements were observed in the terrain F1-score (0.2246 vs. 0.5289). As buffer size increased, all metrics improved noticeably. With a 25-m buffer, the predicted DEM achieved an IoU of 0.6274 compared with 0.3781 for SRTM, and an F1-score of 0.7711 compared with 0.5487 for SRTM.

The same tendency was observed across all metrics, in which the accuracy of the predicted DEM consistently surpassed that of the SRTM-extracted stream network.

Likewise, according to the metrics in Table 7, the predicted DEM in bare soil landscapes also facilitated the extraction of a more accurate stream network compared to SRTM, as is evident from the IoU of extracted streams. The predicted DEM increased the IoU from 0.1183 to 0.2176. Similar improvements are observed in the terrain F1-score (0.2116 vs. 0.3574). As the buffer size increased, all metrics improved. With a 25-m buffer, the predicted DEM achieved an IoU of 0.4703 compared to 0.4218 for SRTM, and an F1-score of 0.6397 compared to 0.5934 for SRTM. The same tendency of the predicted DEM consistently surpassing the stream network extracted from the SRTM was observed across all metrics.

Although the MAE and RMSE of the natural vegetated landscapes were higher, the extracted stream networks in those landscapes were more accurate. Note that Diamond Fork Canyon is steeper, and compared to Casa Diablo Mountain, it is characterized by higher network density (14 km/km² vs. 11 km/km²) and a higher mean slope (59.73° vs. 32.23°).

Three large-scale seamless DEMs are visually presented in Figure 13 for the Denver area in Colorado, in Figure 14 for the Escalante River region in Utah and in Figure 15 for the Dead Sea in Israel. The quality of the DEMs is illustrated in the zoomed-in windows. Buildings and tree footprints are clearly visible in the 30-cm predicted DEM for Denver, small streams and tributaries are clearly depicted in the 60-cm predicted DEM for the Escalante River and sinkholes and streams in 15-cm predicted DEM in the Dead Sea shore. The 30-m SRTM of both of these areas, however, did not capture such fine details. Moreover, tens of thousands of patches were successfully reconstructed into a seamless DEM. There is no visible evidence of patch boundaries. Global features, such as continuous stream networks that span many patches, are coherently preserved in the final DEM.

3.5. Comparison to DEMSR methods

Although our framework does not employ SR reconstruction, we compared our results to those obtained using the main DEM improvement approach, SR-DEM (Zhang and Yu, 2022b). We identified a comparable dataset with reported results for this comparison. Current multi-modal SR methods typically use an upscaling factor of 4; consequently, the recently proposed MFSR model produces a fixed output resolution of 7.5 m (upscaled from 30 m), whereas our method achieves a finer resolution of 5 m corresponding to the RGB resolution provided in the DEM-OPT-Depth SR dataset (Huang et al., 2025). The values of RMSE as reported from various SR models on the DEM-OPT-Depth SR dataset are as follows: Bicubic – 14.891 m, SR-CNN – 8.346 m, ESRGAN – 7.931 m, TfaSR – 7.356 m, SRFormer – 7.741 m, and MFSR – 5.544 m (Huang et al., 2025). Using a publicly available subset of this dataset, our fine-tuned model achieved an RMSE of 5.535 m using just 33% of the data for fine-tuning, exceeding the reported results.

4. Discussion

4.1. Performance using different prompts

Prompt engineering studies involve the optimization of instruction (prompt) design to guide a generative AI model to pro-

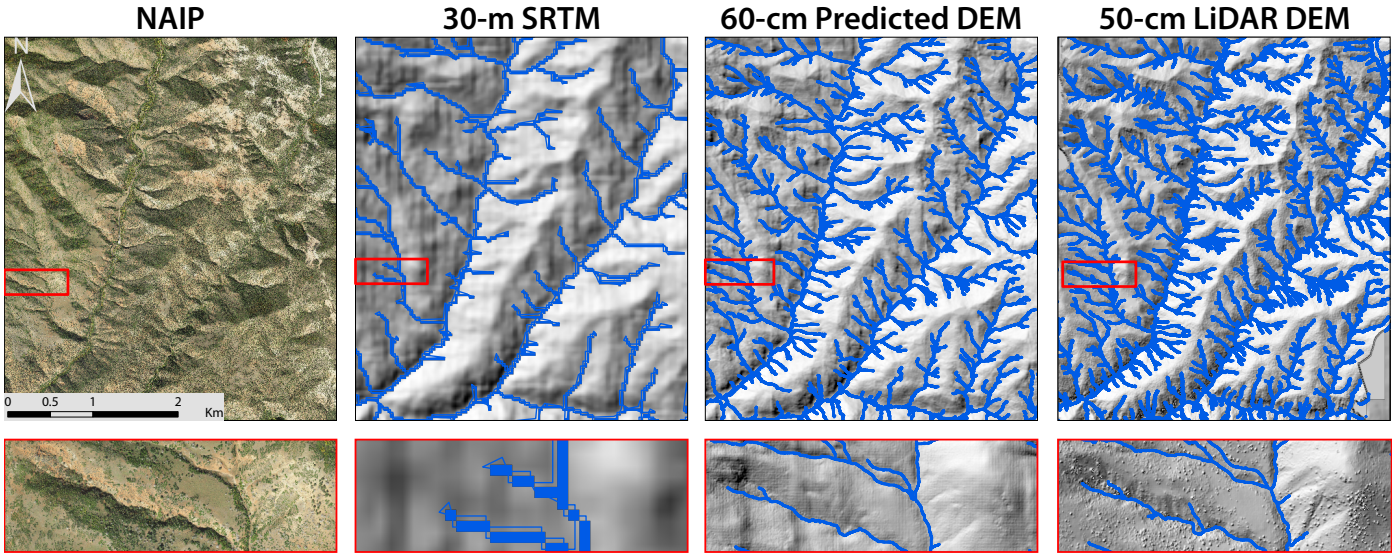


Figure 11: Seamless hillshaded DEM estimation showing the stream network calculated over the entire natural vegetated Diamond Fork Canyon site. Patch stitching did not affect the hydrological analysis, and the detail of the predicted DEM was a stream network that was visually comparable to that obtained with the 50-cm LiDAR DEM, as can be seen in the red zoomed-in visualization.

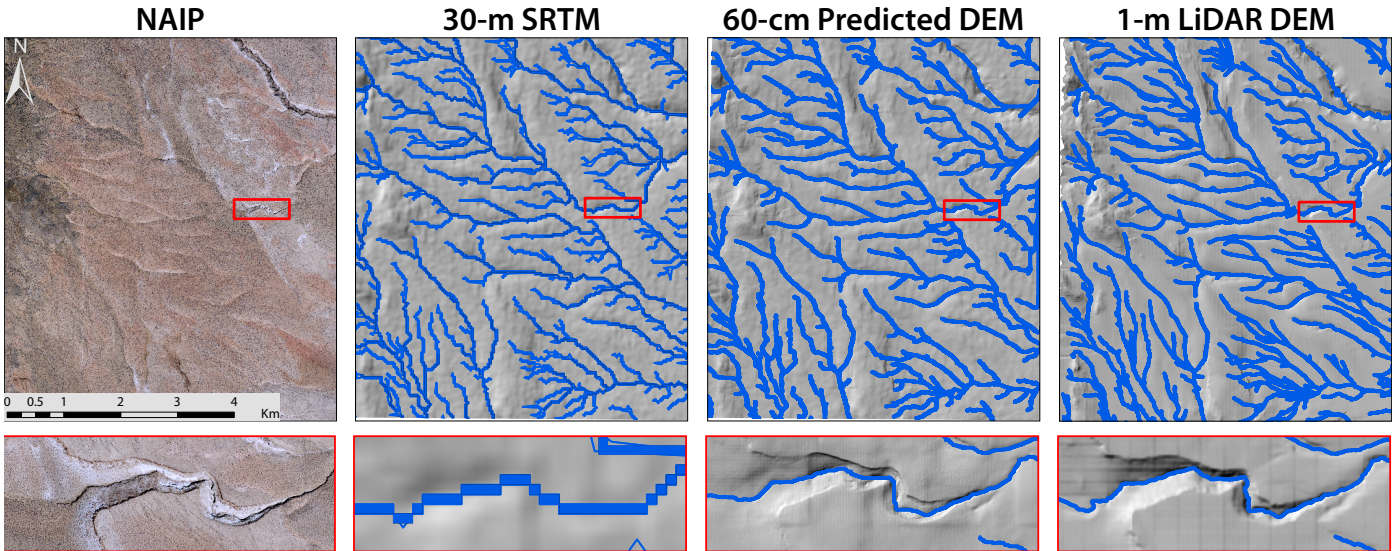


Figure 12: Visual Evaluation – Seamless hillshaded DEM estimation showing the stream network calculated over the entire natural bare terrain in the Casa Diablo Mountain site. Patch stitching did not affect the hydrological analysis, and the detail of the predicted DEM was a stream network visually comparable to the 1 m LiDAR DEM, as can be seen in the red zoomed-in visualization.

Table 6: Accuracy assessment of the extracted stream networks at the natural vegetated evaluation site (Diamond Fork Canyon), using three buffer distances: 5 m, 10 m, and 25 m.

	5 m		10 m		25 m	
	Predicted DEM	SRTM	Predicted DEM	SRTM	Predicted DEM	SRTM
IoU	0.3595	0.1265	0.4723	0.2269	0.6274	0.3781
Precision	0.6085	0.2905	0.7326	0.4685	0.8603	0.7368
Recall	0.4677	0.1831	0.5706	0.3056	0.6986	0.4371
F1-score	0.5289	0.2246	0.6416	0.3699	0.7711	0.5487
Accuracy	0.9077	0.8599	0.8773	0.7996	0.8349	0.7138

duce the desired output (Sahoo et al., 2024; Chen et al., 2024). Prompts were proven to be an effective paradigm in AI, providing crucial information, particularly in large language models (LLMs) and in foundation vision models, such as the Segment

Anything Model (SAM) (Ravi et al., 2024). The recent integration of prompts into MDE shows that they serve as valuable metric information. As demonstrated, PromptDA outperforms all existing MDE methods (Lin et al., 2025). In con-

Table 7: Accuracy assessment of the extracted stream networks at the natural bare evaluation site (Casa Diablo Mountain), using three buffer distances: 5 m, 10 m, and 25 m.

	5 m		10 m		25 m	
	Predicted DEM	SRTM	Predicted DEM	SRTM	Predicted DEM	SRTM
IoU	0.2176	0.1183	0.3083	0.2181	0.4703	0.4218
Precision	0.4047	0.1750	0.5256	0.2932	0.7029	0.5194
Recall	0.3201	0.2676	0.4272	0.4600	0.5869	0.6919
F1-score	0.3574	0.2116	0.4713	0.3581	0.6397	0.5934
Accuracy	0.9354	0.8881	0.9064	0.8389	0.8581	0.7965

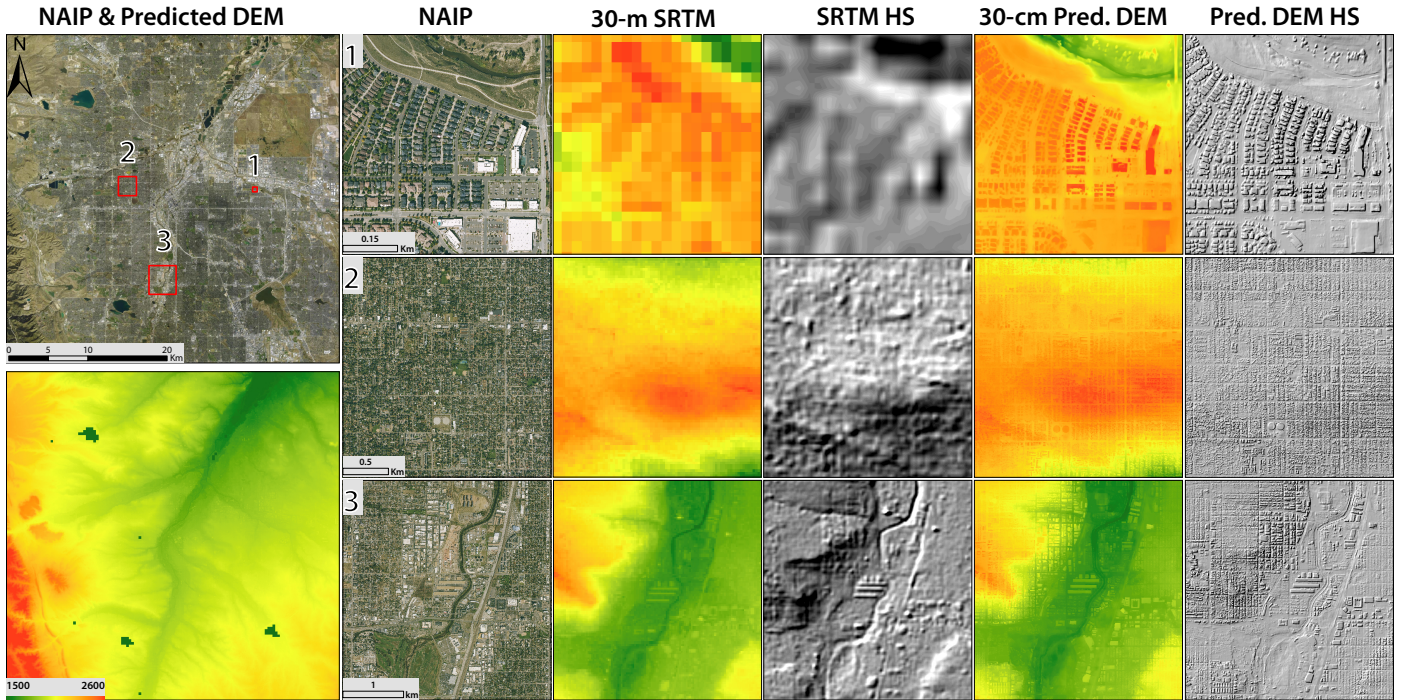


Figure 13: Visual Evaluation: Seamless hillshaded DEM estimation over the Denver, Colorado, urban landscape. Patch stitching is not visible, and the detail of the predicted DEM is visually comparable to that of the 30-m SRTM DEM, as can be seen in the red zoomed-in visualization.

trast to ground-level images, in which predictions are typically performed on a single image processed once by the model, remote sensing DEM estimation involves large images that must be processed in patches (Chen et al., 2025). Prompts offer an excellent opportunity to create seamless DEMs with globally contextualized patches.

In this study, we observed that the source of the prompts affects prediction accuracy. Predictions improved as prompt RMSE decreased and spatial resolution increased. SRTM prompts led to less accurate predictions compared with fused prompts that used holed HR-DEMs combined with SRTM (see Table 3 vs Table 4). HR-DEMs provided more accurate absolute and local feature information, even outside the holed regions, resulting in improved predictions in the predicted voids, particularly in urban and bare landscapes. The lower performance obtained in vegetated landscapes can be attributed to the large discrepancy between the SRTM and the HR-DEM in the holed areas, which caused significantly discontinuous prompts. Moreover, the best predictions were made using HR-DTM prompts, which allowed the framework to estimate only the fine features, such as buildings and vegetation, while the terrain was provided with high accuracy (see Fig. 10 and Table 5).

4.2. Performance in different landscape types

The prompt-based framework was evaluated across three landscape types with varying terrain complexity. As a result, the reliability of the prompts, which were derived from the global 30-m SRTM data, varied depending on the terrain. Specifically, the accuracy of SRTM was lower in complex environments such as urban and vegetated areas compared to bare landscapes. This reduction in accuracy has also been noted in several previous studies (Su and Guo, 2014; Gamba et al., 2002). Specifically, the vertical error of the SRTM increased significantly in regions characterized by the presence of natural or artificial features on bare earth (Hofman et al., 2006). In vegetated landscapes, the elevation values obtained are typically between the elevation of the land surface and that of the canopy top, and similar findings were reported in dense urban landscapes (Colosimo et al., 2009). We observed similar trends in our dataset. For instance, the RMSE of the SRTM compared with the 50 cm LiDAR was 7.275 m in the vegetated Diamond Fork Canyon and 3.434 m in the Provo urban area, while in the bare landscape of Casa Diablo Mountain, it was only 2.871 m. These inconsistencies complicate the generalizability of the framework in different regions, leading to varied prompt accuracy and model performance in different landscapes (see

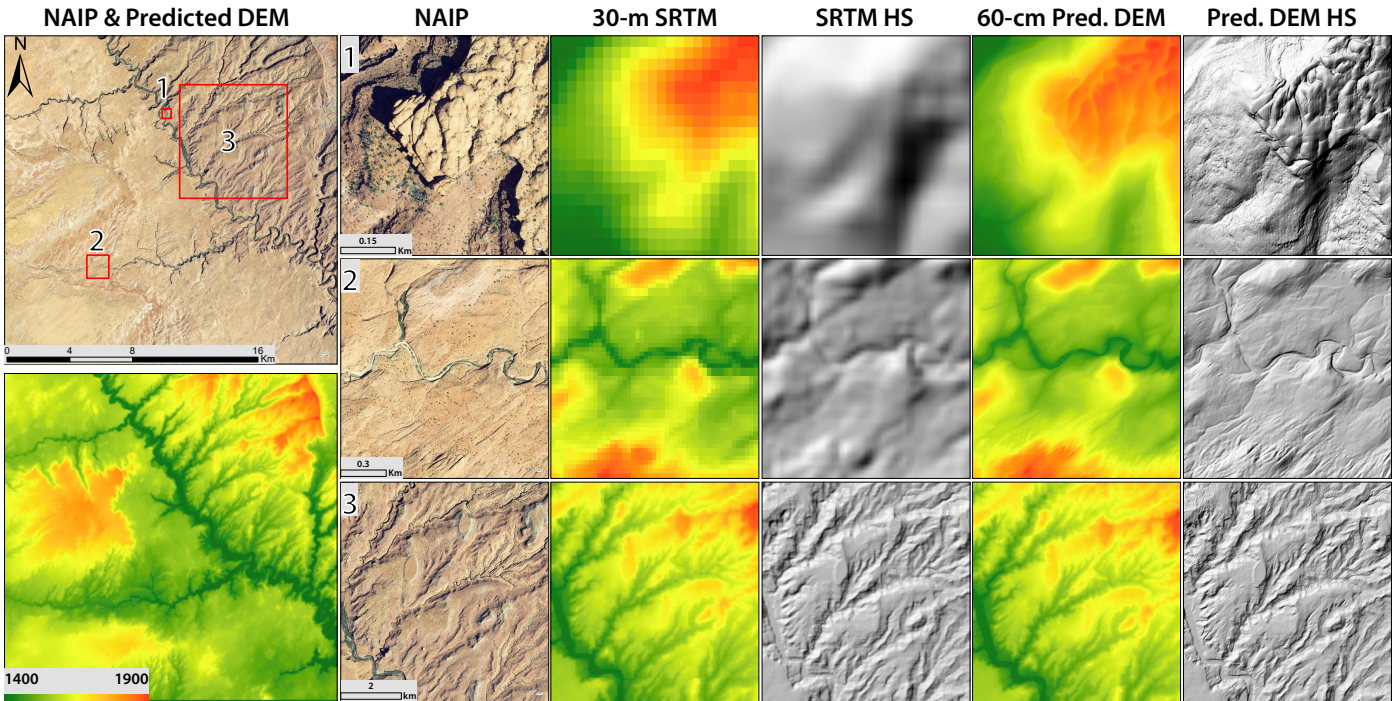


Figure 14: Visual Evaluation: Seamless hillshaded DEM estimation for the Escalante River region in Utah. Patch stitching is not visible, and the detail of the predicted DEM is visually comparable to that of the 30-m SRTM DEM, as can be seen in the red zoomed-in visualization.

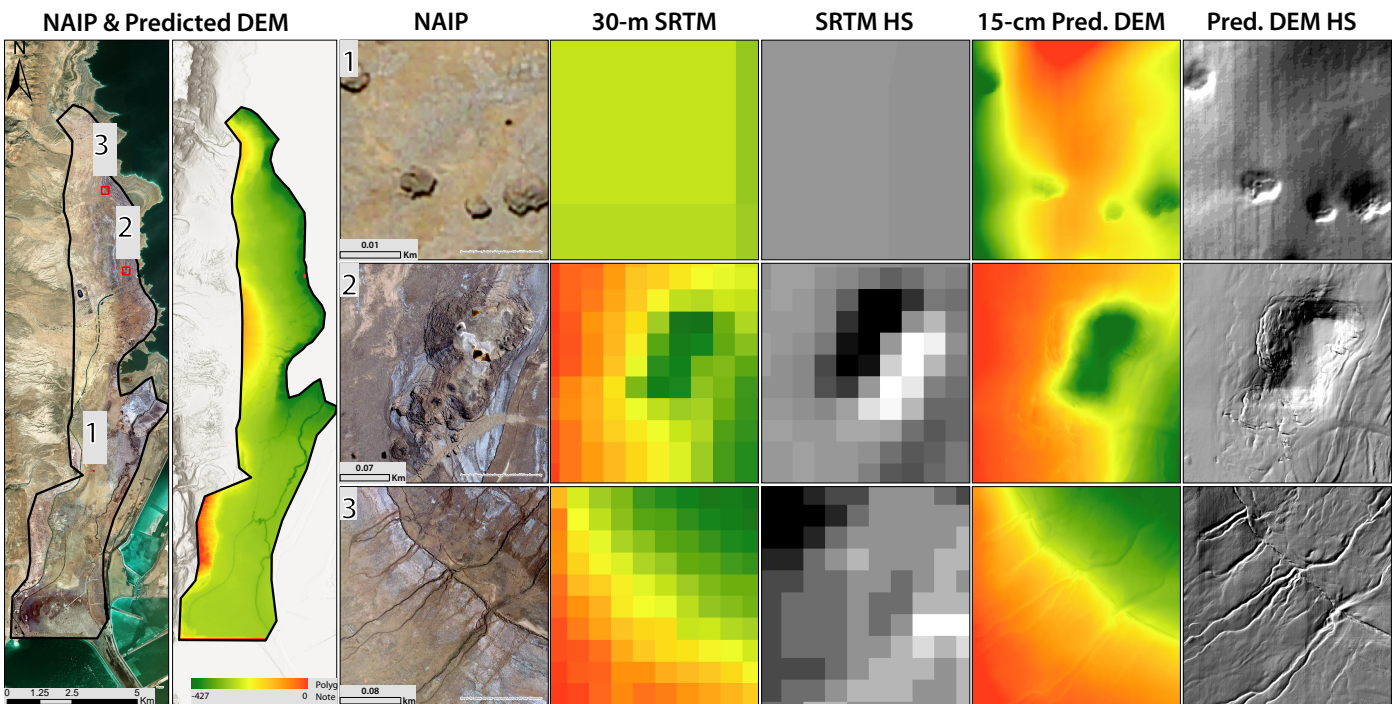


Figure 15: Visual Evaluation: Seamless hillshaded DEM estimation over the entire Dead Sea shore. Patch stitching is not visible, and the detail of the predicted DEM is visually comparable to that of the 30-m SRTM DEM, as can be seen in the red zoomed-in visualization.

Table 3). Consequently, we fine-tuned the model separately for each of the three landscape types using three distinct pretrained models.

Although the accuracy of SRTM diminishes in complex terrains, MDE offers superior performance in capturing fine features, especially through the shading of steep elements (Florea and Nedevschi, 2025; Song et al., 2025; Tian et al., 2024). As

a result, the most significant improvements were observed in the elevation and slope accuracy for vegetated landscapes, with an 18% improvement in MAE over SRTM. This result is consistent with the reported performance of MDE, which is more precise, particularly in delineating building and tree contours and in capturing local elevation changes (Hong et al., 2025; Liu et al., 2020). Another observation supporting the superior

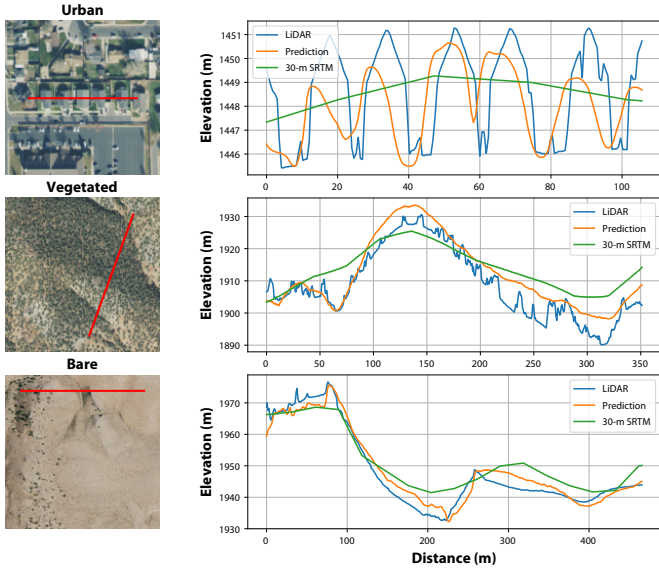


Figure 16: DEM estimation with SRTM, HR-LiDAR DEM, and predicted elevation profiles. Although SRTM missed fine features, the model estimation captured buildings and small streams in both the vegetated and bare terrain landscapes.

performance of MDE in shaded regions is that the predicted stream network in the steep, vegetated landscape of Diamond Fork Canyon (see Fig. 11) was more accurate than the predicted features in the flatter Casa Diablo Mountain site (see Fig. 12). This suggests that, despite initial inaccuracies in the prompts for vegetated landscapes, shadows facilitated the model’s inference of more reliable topographic information that resulted in greater local precision.

4.3. MDE vs SR

Super-resolution (SR) approaches were used in a variety of studies to improve DEM (Zhang and Yu, 2022a). Although monocular depth estimation is attracting increased attention in remote sensing studies, they are still rarely used in studies of open environments, particularly in the context of hydrological and geomorphological processes such as hillslope erosion and stream network extraction (Tangellapalli et al., 2024; Rafaeli et al., 2025). Note that there is a critical conceptual difference between SR and MDE. Although MDE is superior to SR in terms of accuracy and resolution, it has been less widely adopted for DEM enhancement due to its lack of global context (Florea and Nedeveschi, 2025).

More recently, a multi-modal fusion super-resolution (MFSR) framework was used to integrate monocular depth models into the super-resolution process. The proposed MFSR approach utilized predicted zero-shot relative depth to capture complementary structural terrain information, thereby enhancing elevation detail. The experimental results demonstrated a 24.63% improvement in RMSE compared with state-of-the-art super-resolution techniques (Huang et al., 2025). The latest MFSR method represents a significant step toward integrating monocular foundation models through a proposed multimodal framework. Although the MDE output reached a resolution comparable to the RGB data (5 m in the MFSR dataset), the model was still constrained by a fixed 4× upscaling factor (i.e., from 30-m to 7.5-m). This architectural limitation hinders its

ability to reconstruct fine-scale terrain features and to generalize across different RGB sources (Huang et al., 2025).

Considering the shortcomings mentioned above of different DEMSRs, deep learning-based MDE models constitute an alternative by quantifying depth from a single RGB image using training sets (Zhao et al., 2020). Rather than estimate depth through low-to-high resolution (LR-to-HR) translation, MDE models leverage scene-aware representation using RGB information (Yang et al., 2024a). In addition, MDE models are not constrained by fixed upscaling factors; instead, they produce depth estimates at the resolution of the RGB input (see Fig. 16).

Monocular depth estimation (MDE) has been applied in the remote sensing (RS) field, where it is often referred to as monocular height estimation (MHE). Height estimation has been used in both agricultural and urban environments (Zhang et al., 2024)—for example, to estimate agricultural canopy height using a fine-tuned Depth Anything model. More recently, Depth Anything was applied for the first time to height estimation in urban remote sensing scenes, marking a significant milestone in its development (Hong et al., 2025). Nonetheless, MDE predictions still operate in a local context rather than a global one, which limits their ability to capture regional elevation trends at broader scales (Song et al., 2025).

Unlike ground-level imagery, where predictions are typically performed on single images processed once by the model, remote sensing DEM prediction requires processing large images in patches (Chen et al., 2025). Until now, MDE has lacked a means of incorporating global elevation context (Hong et al., 2025). In the context of DEM enhancement, prompts offer a significant opportunity to estimate elevation across patches while preserving absolute elevation values (e.g., above sea level), potentially enabling the generation of seamless DEMs with global consistency.

We show that prompt-based MDE is capable of improving resolution 50× to 200× by relying on globally available elevation sources such as SRTM. MDE uses contextual depth cues to generalize to unseen regions, and it produces seamless DEMs. Moreover, in terms of RMSE values, our approach outperforms SR methods, as we demonstrated on the DEM-OPT-Depth SR dataset.

4.4. Large-scale application

As mentioned earlier, HR-DEM datasets are critical for environmental studies and urban planning. Indeed, in many cases, the use of hazard information generated from available LR-DEMs was dangerously misleading (Simpson et al., 2015). For example, LR-DEMs can present major challenges because of their substantial vertical error and the fact that they measure surface elevation, including treetops and building tops, rather than bare earth, a shortcoming that can underestimate flood risk (Muthusamy et al., 2021).

HR-DEMs in the United States are provided primarily by the USDA Natural Resources Conservation Service (NRCS) and the USGS 3D Elevation Program (3DEP) (Survey, 2025). Nearly 80% of the contiguous United States (CONUS) has been mapped with 1-m LiDAR-derived DEMs, while for some regions, sub-meter DEMs are available (Survey, 2025). In addition to the issue of spatial coverage, these HR-DEMs have temporal limitations. For example, annual nationwide updates have not been implemented, in contrast to the high frequency

of RGB image acquisitions provided by the NAIP or by HR-satellite imagery (Sugarbaker et al., 2017).

The extensive, high-resolution DEM coverage of the United States notwithstanding (≤ 1 m), global coverage is still lacking, which is due primarily to the high costs involved (Zand-salimi et al., 2025). Although airborne surveys are not feasible in low-resource regions, a variety of global or near-global digital elevation models has become freely accessible in the last two decades, along with high-resolution satellite imagery (Pu and Landry, 2012). Notably, many studies have demonstrated the efficacy of machine learning techniques in refining low-resolution DEMs (LR-DEMs) and correcting inherent biases (Yu et al., 2025a; Yue et al., 2024; Tao et al., 2024; Kim et al., 2020; Tian and Shan, 2024). Compared with LiDAR or photogrammetric acquisition methods, deep learning approaches based on these widely available datasets are significantly more resource-efficient, both operationally and computationally, and they can even be applied on the end user's personal computer (Ruiz-Lendínez et al., 2023).

Our results demonstrate that it is possible to generate high-resolution, seamless DEMs at a large scale, as evidenced in both the evaluation and application phases. The proposed framework has the potential to increase global high-resolution DEM coverage and improve temporal resolution in areas where LiDAR is already available. In addition to producing accurate and finely detailed elevation models, the proposed method is also resource-efficient. Specifically, on a single GPU, the framework can generate DEMs at a rate of 150 km² per hour. Using a high-performance computing cluster, the total processing time can be significantly reduced. For instance, using 10 computer nodes in parallel, the processing time for generating a DEM that covers the entire CONUS would be approximately ten months.

5. Conclusions

This study introduces a novel framework that leverages prompt-based MDE to generate high-resolution, seamless, and metric DEMs across diverse landscapes. It is designed to address three key tasks: HR-DEM estimation, DEM void filling, and DEM updating.

Our extensive evaluation across three diverse sites in the U.S.—representing urban, natural vegetated, and bare land landscapes—shows that our framework achieved exceptional performance, and compared with SRTM, it improved the MAE by 14%, 18%, and 3% for urban, vegetated, and bare land regions, respectively. It surpassed traditional super-resolution approaches both in upscaling capability and accuracy, thus establishing a new paradigm in DEM enhancement. By leveraging MDE with globally contextualized patches, our framework enabled seamless DEM reconstruction, making it suitable for downstream geospatial applications such as hydrological analysis, urban development monitoring and urban climate studies.

Future Developments: Although this research used publicly available data such as SRTM and NAIP, both the prompts and RGB imagery can be sourced from alternative datasets. For example, the upscaling requirement could be smaller—such as from airborne LiDAR to drone-resolution inputs, moreover, high-resolution satellite imagery could also serve as a crucial step toward global mapping for the first time using deep learning-based monocular depth estimation (MDE). Object-based evaluation using mapped features such as buildings and

tree canopies can further enhance our understanding of accuracy across different environments at the object level. Future improvements may also involve advances in model architecture, loss functions, and multi-modality, including the integration of multispectral data.

This work positions MDE as a powerful alternative to traditional SR approaches for DEM enhancement, bridging scene-aware representations with topographic settings. It opens new avenues for the generation of prompt-based, context-aware MDE, particularly in heterogeneous and challenging terrains.

Acknowledgment

We thank the Ministry of Agriculture, Chief Scientist Program, grant number 16-17-0005, 2022, and the Negev Scholarship from the Kreitman School of Ben-Gurion University of the Negev for supporting Osher Rafaeli's PhD studies.

References

- , 2025. Bishop, ca: Morphological characteristics of the bishop tuff. Distributed by OpenTopography. URL: <https://doi.org/10.5069/G9J1012J>, doi:10.5069/G9J1012J, accessed: 2025-06-03.
- , 2025. Lake bonneville, utah. Distributed by OpenTopography. URL: <https://doi.org/10.5069/G9JW8BTS>, doi:10.5069/G9JW8BTS, accessed: 2025-06-03.
- , 2025. Opentopography: High-resolution topography data and tools. <https://opentopography.org>. Accessed: 2025-06-03.
- , 2025. State of utah acquired lidar data - wasatch front. Distributed by OpenTopography. URL: <https://doi.org/10.5069/G9TH8JNQ>, doi:10.5069/G9TH8JNQ, accessed: 2025-06-03.
- Bhardwaj, A., Sam, L., Bhardwaj, A., Martín-Torres, F.J., 2016. Lidar remote sensing of the cryosphere: Present applications and future prospects. *Remote Sensing of Environment* 177, 125–143. URL: <https://www.sciencedirect.com/science/article/pii/S0034425716300591>, doi:<https://doi.org/10.1016/j.rse.2016.02.031>.
- Birkl, R., Wofk, D., Müller, M., 2023a. Midas v3. 1—a model zoo for robust monocular relative depth estimation. *arXiv preprint arXiv:2307.14460*.
- Birkl, R., Wofk, D., Müller, M., 2023b. Midas v3.1 – a model zoo for robust monocular relative depth estimation. URL: <https://arxiv.org/abs/2307.14460>, arXiv:2307.14460.
- Cambrin, D.R., Corley, I., Garza, P., 2024. Depth any canopy: Leveraging depth foundation models for canopy height estimation. *arXiv preprint arXiv:2408.04523*.
- Cao, H., Xiong, L., Wang, H., Zhao, F., Strobl, J., 2025. hydrological knowledge. *International Journal of Geographical Information Science* 39, 301–325.
- Chen, K., Liu, C., Chen, B., Li, W., Zou, Z., Shi, Z., 2025. Dynamicvis: An efficient and general visual foundation model for remote sensing image understanding. *arXiv preprint arXiv:2503.16426*.
- Chen, K., Liu, C., Chen, H., Zhang, H., Li, W., Zou, Z., Shi, Z., 2024. Rsprompter: Learning to prompt for remote sensing instance segmentation based on visual foundation model. *IEEE Transactions on Geoscience and Remote Sensing* 62, 1–17.
- Colomina, I., Molina, P., 2014. Unmanned aerial systems for photogrammetry and remote sensing: A review. *ISPRS Journal of photogrammetry and remote sensing* 92, 79–97.
- Colosimo, G., Crespi, M., De Vendictis, L., Jacobsen, K., et al., 2009. Accuracy evaluation of srtm and aster dsms, in: *Proceedings of the 29th EARSeL Symposium, Chania, Greece*, pp. 15–18.
- Cutler, M., 2008. Comparison of remotely sensed water stages from lidar, topographic contours and srtm. *ISPRS journal of photogrammetry and remote sensing* 63, 283–296.
- Dorshow, W., 2019. 3d landscape reconstruction and land use modeling, chaco canyon, nm 2016. National Center for Airborne Laser Mapping (NCALM). Distributed by OpenTopography. URL: <https://doi.org/10.5069/G9XG9P8D>, doi:10.5069/G9XG9P8D, accessed: 2025-06-03.
- Federal Geographic Data Committee, 1998. Fgdc-std-001-1998: Geospatial metadata. URL: <https://www.fgdc.gov>, accessed: 2025-06-08.

- Florea, H., Nedevschi, S., 2025. Tandepth: Leveraging global dems for metric monocular depth estimation in uavs. *IEEE Journal of Selected Topics in Applied Earth Observations and Remote Sensing* 18, 5445–5459. URL: <http://dx.doi.org/10.1109/JSTARS.2025.3531984>, doi:10.1109/jstars.2025.3531984.
- Gamba, P., Dell'Acqua, F., Houshmand, B., et al., 2002. Srtm data characterization in urban areas. *International Archives of Photogrammetry Remote Sensing and Spatial Information Sciences* 34, 55–58.
- Guth, P.L., Van Niekerk, A., Grohmann, C.H., Muller, J.P., Hawker, L., Florinsky, I.V., Gesch, D., Reuter, H.I., Herrera-Cruz, V., Riazanoff, S., et al., 2021. Digital elevation models: Terminology and definitions. *Remote Sensing* 13, 3581.
- Hermann, M., Ruf, B., Weinmann, M., Hinz, S., 2020. Self-supervised learning for monocular depth estimation from aerial imagery. *ISPRS Annals of the Photogrammetry, Remote Sensing and Spatial Information Sciences V-2-2020*, 357–364. URL: <http://dx.doi.org/10.5194/isprs-annals-v-2-2020-357-2020>, doi:10.5194/isprs-annals-v-2-2020-357-2020.
- Hofton, M., Dubayah, R., Blair, J.B., Rabine, D., 2006. Validation of srtm elevations over vegetated and non-vegetated terrain using medium footprint lidar. *Photogrammetric Engineering & Remote Sensing* 72, 279–285.
- Hong, Z., Wu, T., Xu, Z., Zhao, W., 2025. Depth2elevation: Scale modulation with depth anything model for single-view remote sensing image height estimation. *IEEE Transactions on Geoscience and Remote Sensing*.
- Huang, W., Sun, Q., Guo, W., Xu, Q., Ma, J., Gao, T., Yu, A., 2024. Dem super-resolution guided by shaded relief using attention-based fusion. *International Journal of Applied Earth Observation and Geoinformation* 132, 104014. URL: <https://www.sciencedirect.com/science/article/pii/S1569843224003686>, doi:<https://doi.org/10.1016/j.jag.2024.104014>.
- Huang, W., Sun, Q., Guo, W., Xu, Q., Wen, B., Gao, T., Yu, A., 2025. Multi-Modal DEM Super-Resolution Using Relative Depth: A New Benchmark and Beyond. <https://ssrn.com/abstract=5123516>. Available at SSRN: <https://ssrn.com/abstract=5123516> or <http://dx.doi.org/10.2139/ssrn.5123516>.
- Jones, J., 2018. Mapping of diamond fork river, ut 2017. National Center for Airborne Laser Mapping (NCALM). Distributed by OpenTopography. URL: <https://doi.org/10.5069/G94T6G9J>, doi:10.5069/G94T6G9J. accessed: 2025-06-03.
- Kim, D.E., Liang, S.Y., Gourbesville, P., Andres, L., Liu, J., 2020. Simple-yet-effective srtm dem improvement scheme for dense urban cities using ann and remote sensing data: Application to flood modeling. *Water* 12. URL: <https://www.mdpi.com/2073-4441/12/3/816>, doi:10.3390/w12030816.
- Lin, H., Peng, S., Chen, J., Peng, S., Sun, J., Liu, M., Bao, H., Feng, J., Zhou, X., Kang, B., 2025. Prompting depth anything for 4k resolution accurate metric depth estimation. URL: <https://arxiv.org/abs/2412.14015>, arXiv:2412.14015.
- Liu, C.J., Krylov, V.A., Kane, P., Kavanagh, G., Dahyot, R., 2020. Im2elevation: Building height estimation from single-view aerial imagery. *Remote Sensing* 12. URL: <https://www.mdpi.com/2072-4292/12/17/2719>, doi:10.3390/rs12172719.
- Ming, Y., Meng, X., Fan, C., Yu, H., 2021. Deep learning for monocular depth estimation: A review. *Neurocomputing* 438, 14–33. URL: <https://doi.org/10.1016/j.neucom.2020.12.089>, doi:<https://doi.org/10.1016/j.neucom.2020.12.089>.
- Muthusamy, M., Casado, M.R., Butler, D., Leinster, P., 2021. Understanding the effects of digital elevation model resolution in urban fluvial flood modelling. *Journal of Hydrology* 596, 126088. URL: <https://www.sciencedirect.com/science/article/pii/S0022169421001359>, doi:<https://doi.org/10.1016/j.jhydrol.2021.126088>.
- NASA Shuttle Radar Topography Mission (SRTM), 2013. Shuttle radar topography mission (srtm) global. Distributed by OpenTopography. URL: <https://doi.org/10.5069/G9445JDF>, doi:10.5069/G9445JDF. accessed: 2025-06-03.
- Panangian, D., Bittner, K., 2024. Real-gdsr: Real-world guided dsm super-resolution via edge-enhancing residual network. *ISPRS Annals of the Photogrammetry, Remote Sensing and Spatial Information Sciences X-2-2024*, 185–192. URL: <https://isprs-annals.copernicus.org/articles/X-2-2024/185/2024/>, doi:10.5194/isprs-annals-X-2-2024-185-2024.
- Passalacqua, P., 2015. Austin, tx, rapid response, 2015 airborne lidar survey. National Center for Airborne Laser Mapping (NCALM). Distributed by OpenTopography. URL: <https://doi.org/10.5069/G9FB5115>, doi:10.5069/G9FB5115. accessed: 2025-06-03.
- Pu, R., Landry, S., 2012. A comparative analysis of high spatial resolution ikonos and worldview-2 imagery for mapping urban tree species. *Remote Sensing of Environment* 124, 516–533.
- Rafaeli, O., Svoray, T., Nahlieli, A., 2025. Sinksam-net: Knowledge-driven self-supervised sinkhole segmentation using topographic priors and segment anything model. *ISPRS Journal of Photogrammetry and Remote Sensing* 228, 1–15. URL: <https://www.sciencedirect.com/science/article/pii/S0924271625002618>, doi:<https://doi.org/10.1016/j.isprsjprs.2025.06.035>.
- Ranftl, R., Bochkovskiy, A., Koltun, V., 2021. Vision transformers for dense prediction, in: *Proceedings of the IEEE/CVF international conference on computer vision*, pp. 12179–12188.
- Ravi, N., Gabeur, V., Hu, Y.T., Hu, R., Ryali, C., Ma, T., Khedr, H., Rädle, R., Rolland, C., Gustafson, L., Mintun, E., Pan, J., Vasudev Alwala, K., Carion, N., Wu, C.Y., Girshick, R., Dollár, P., Feichtenhofer, C., Fair, M., 2024. SAM 2: Segment Anything in Images and Videos. Technical Report.
- Richardt, C., Pritch, Y., Zimmer, H., Sorkine-Hornung, A., 2013. Megastereo: Constructing high-resolution stereo panoramas, in: *2013 IEEE Conference on Computer Vision and Pattern Recognition*, pp. 1256–1263. doi:10.1109/CVPR.2013.166.
- Rodriguez, E., Morris, C.S., Belz, J.E., 2006. A global assessment of the srtm performance. *Photogrammetric Engineering & Remote Sensing* 72, 249–260.
- Ruiz-Lendínez, J.J., Ariza-López, F.J., Reinoso-Gordo, J.F., Ureña-Cámara, M.A., and, F.J.Q.R., 2023. Deep learning methods applied to digital elevation models: state of the art. *Geocarto International* 38, 2252389. URL: <https://doi.org/10.1080/10106049.2023.2252389>, doi:10.1080/10106049.2023.2252389, arXiv:<https://doi.org/10.1080/10106049.2023.2252389>.
- Sahoo, P., Singh, A.K., Saha, S., Jain, V., Mondal, S., Chadha, A., 2024. A systematic survey of prompt engineering in large language models: Techniques and applications. arXiv preprint arXiv:2402.07927.
- Simpson, A.L., Balog, S., Moller, D.K., Strauss, B., Saito, K., 2015. An urgent case for higher resolution digital elevation models in the world's poorest and most vulnerable countries. *Frontiers in Earth Science* Volume 3 - 2015. URL: <https://www.frontiersin.org/journals/earth-science/articles/10.3389/feart.2015.00050>, doi:10.3389/feart.2015.00050.
- Song, J., Chen, H., Yokoya, N., 2025. Enhancing monocular height estimation via sparse lidar-guided correction. arXiv preprint arXiv:2505.06905.
- Su, Y., Guo, Q., 2014. A practical method for srtm dem correction over vegetated mountain areas. *ISPRS Journal of Photogrammetry and Remote Sensing* 87, 216–228. URL: <https://www.sciencedirect.com/science/article/pii/S0924271613002712>, doi:<https://doi.org/10.1016/j.isprsjprs.2013.11.009>.
- Sugarbaker, L.J., Eldridge, D.F., Jason, A.L., Lukas, V., Saghy, D.L., Stoker, J.M., Thunen, D.R., 2017. Status of the 3D elevation program, 2015. Technical Report. US Geological Survey.
- Survey, U.G., 2025. 3dep lidar point cloud, version 1.0. Available from The National Map on 2025-06-20. URL: <https://www.usgs.gov/programs/national-geospatial-program/national-map>. accessed: 2025-06-20.
- Svoray, T., 2004. Integrating automatically processed spot hrv pan imagery in a dem-based procedure for channel network extraction. *International Journal of Remote Sensing* 25, 3541–3547. URL: <https://doi.org/10.1080/01431160410001684992>, doi:10.1080/01431160410001684992.
- Svoray, T., Sela, S., Chen, L., Assouline, S., 2021. Lateral flow and contributing area control vegetation cover in a semiarid environment. *Water Resources Research* 57, e2021WR030998. doi:<https://doi.org/10.1029/2021WR030998>. e2021WR030998 2021WR030998.
- Tangellapalli, S.A., Singh Sangha, H., Peschel, J., Duncan, B.A., 2024. Assessing monocular depth estimation networks for uas deployment in rainforest environments, in: *2024 IEEE/RSJ International Conference on Intelligent Robots and Systems (IROS)*, pp. 5024–5031. doi:10.1109/IROS58592.2024.10802125.
- Tao, P., Li, Z., Hu, Z., Xiong, Q., Chen, Q., 2024. A simple adaptive dem void filling method based on raster distance transform. *IEEE Geoscience and Remote Sensing Letters*.
- Tian, F., Zhou, P., Li, C., Wang, C., 2024. Shadow constrained dem refinement based on differentiable rendering, in: *2024 IEEE International Conference on Multimedia and Expo (ICME)*, pp. 1–6. doi:10.1109/ICME57554.2024.10687819.
- Tian, X., Shan, J., 2024. Icesat-2 controlled integration of gedi and srtm data for large-scale digital elevation model generation. *IEEE Transactions on Geoscience and Remote Sensing* 62, 1–14. doi:10.1109/TGRS.2024.3389821.
- U.S. Geological Survey, 2025. National agriculture imagery program

- (naip). U.S. Geological Survey, EROS Archive. URL: <https://earthexplorer.usgs.gov/>, doi:10.5066/F7QN651G.
- Wang, H., Xiong, L., Hu, G., Cao, H., Li, S., Tang, G., Zhou, L., 2024a. Dem super-resolution framework based on deep learning: decomposing terrain trends and residuals. *International Journal of Digital Earth* 17, 2356121. URL: <https://doi.org/10.1080/17538947.2024.2356121>, doi:10.1080/17538947.2024.2356121, arXiv:<https://doi.org/10.1080/17538947.2024.2356121>.
- Wang, Y., Jin, S., Yang, Z., Guan, H., Ren, Y., Cheng, K., Zhao, X., Liu, X., Chen, M., Liu, Y., Guo, Q., 2024b. Tsr: A transformer-based topography neural network for digital elevation model super-resolution. *IEEE Transactions on Geoscience and Remote Sensing* 62, 1–19. doi:10.1109/TGRS.2024.3360489.
- Wang, Z., Menenti, M., 2021. Challenges and opportunities in lidar remote sensing. *Frontiers in Remote Sensing* 2, 641723.
- Wilson, J.P., 2012. Digital terrain modeling. *Geomorphology* 137, 107–121. URL: <https://www.sciencedirect.com/science/article/pii/S0169555X11001449>, doi:<https://doi.org/10.1016/j.geomorph.2011.03.012>. geospatial Technologies and Geomorphological Mapping Proceedings of the 41st Annual Binghamton Geomorphology Symposium.
- Yang, L., Kang, B., Huang, Z., Xu, X., Feng, J., Zhao, H., 2024a. Depth anything: Unleashing the power of large-scale unlabeled data, in: *Proceedings of the IEEE/CVF Conference on Computer Vision and Pattern Recognition*, pp. 10371–10381.
- Yang, L., Kang, B., Huang, Z., Xu, X., Feng, J., Zhao, H., 2024b. Depth anything: Unleashing the power of large-scale unlabeled data. URL: <https://arxiv.org/abs/2401.10891>, arXiv:2401.10891.
- Yang, L., Kang, B., Huang, Z., Zhao, Z., Xu, X., Feng, J., Zhao, H., 2024c. Depth Anything V2 URL: <http://arxiv.org/abs/2406.09414>.
- Yao, S., Cheng, Y., Yang, F., Mozerov, M.G., 2024. A continuous digital elevation representation model for dem super-resolution. *ISPRS Journal of Photogrammetry and Remote Sensing* 208, 1–13. URL: <https://www.sciencedirect.com/science/article/pii/S0924271624000017>, doi:<https://doi.org/10.1016/j.isprsjprs.2024.01.001>.
- Yu, C., Wang, Q., Zhang, Z., Zhong, Z., Ding, Y., Lai, T., Huang, H., Shen, P., 2025a. Multi-source data joint processing framework for dem calibration and fusion. *International Journal of Applied Earth Observation and Geoinformation* 139, 104484. URL: <https://www.sciencedirect.com/science/article/pii/S1569843225001311>, doi:<https://doi.org/10.1016/j.jag.2025.104484>.
- Yu, J., Li, Y., Bai, X., Yang, R., Cui, M., Wu, H., Li, Z., Su, F., Li, Z., Liang, T., et al., 2025b. A dem super resolution reconstruction method based on normalizing flow. *Scientific Reports* 15, 10681.
- Yue, L., Gao, B., Zheng, X., 2024. Generative dem void filling with terrain feature-guided transfer learning assisted by remote sensing images. *IEEE Geoscience and Remote Sensing Letters*.
- Zandsalimi, Z., Barbosa, S.A., Alemazkoo, N., Goodall, J.L., Shafiee-Jood, M., 2025. Deep learning-based downscaling of global digital elevation models for enhanced urban flood modeling. *Journal of Hydrology* 653, 132687. URL: <https://www.sciencedirect.com/science/article/pii/S0022169425000253>, doi:<https://doi.org/10.1016/j.jhydrol.2025.132687>.
- Zhan, H., Garg, R., Weerasekera, C.S., Li, K., Agarwal, H., Reid, I., 2018. Unsupervised learning of monocular depth estimation and visual odometry with deep feature reconstruction, in: *Proceedings of the IEEE Conference on Computer Vision and Pattern Recognition (CVPR)*.
- Zhang, J., Li, J., Huang, Y., Wang, Y., Zheng, J., Shen, L., Cao, Z., 2024. Towards robust monocular depth estimation in non-lambertian surfaces. arXiv preprint arXiv:2408.06083.
- Zhang, Y., Yu, W., 2022a. Comparison of dem super-resolution methods based on interpolation and neural networks. *Sensors* 22. URL: <https://www.mdpi.com/1424-8220/22/3/745>, doi:10.3390/s22030745.
- Zhang, Y., Yu, W., 2022b. Comparison of dem super-resolution methods based on interpolation and neural networks. *Sensors* 22, 745.
- Zhao, C., Sun, Q., Zhang, C., Tang, Y., Qian, F., 2020. Monocular depth estimation based on deep learning: An overview. *Science China Technological Sciences* 63, 1612–1627.